

Improving sea level fingerprints associated with future land ice melting

By

Shujing Zhang

Bachelor of Marine and Antarctic Science (Honours),

University of Tasmania,

A thesis submitted in partial fulfilment of the requirements of the Bachelor of
Marine and Antarctic Science with Honours at the Institute for Marine and
Antarctic studies (IMAS), University of Tasmania (July 2020).



UNIVERSITY *of*
TASMANIA



IMAS
INSTITUTE FOR MARINE
& ANTARCTIC STUDIES

Declaration

I declare that all material in this thesis is my own work, and contains no material that has been accepted for the award of any other degree or diploma in any tertiary institution and that, to the best of my knowledge, contains no material previously published or written by another person, except where due reference is made in the text of this thesis.

Shujing Zhang

09 July 2020

Abstract

Mass changes of land ice (e.g., glaciers and ice sheets) lead to geographically variable patterns in regional sea level, also called “sea level fingerprints”. Sea level fingerprints associated with contemporary land ice mass changes can be derived by solving the sea level equation, in which Earth’s elastic response, gravitational and rotational effects are included. However, current sea level fingerprint products are generally limited to coarse resolutions due to high computational cost. Uncertainties in sea level fingerprints also arise due to the limited spatial resolutions at which the ice mass changes are represented and the choice of 1-D elastic Earth models to represent a complex 3-D Earth. While published work to date has considered the sensitivity of individual coastal cities to entire ice sheets, there are no studies that examine the sensitivity of local near-future sea level projections to mass changes in individual ice sheet basins (e.g., by the end of the 21st century). In our research, we utilize the sea level fingerprint module - ISSM’s Solid Earth and Sea level Adjustment Workbench (ISSM-SESAW), developed by NASA/Jet Propulsion Laboratory (JPL), to provide high-resolution sea level fingerprints in response to future polar ice sheet mass changes in the 21st century under the Representative Concentration Pathway (RCP) 4.5 and 8.5 scenarios. We also explore the sensitivity of sea level fingerprints to different 1-D elastic Earth models and the spatial resolution at which mass change of polar ice sheets is resolved. Furthermore, sea level contributions by individual polar ice sheet basins in the 21st century are also estimated for some coastal cities of interest (e.g., Perth) in this research. Our results show that the sea level fingerprints are effectively insensitive to different crustal structures in 1-D elastic Earth models. However, the resolution at which polar ice sheets are resolved has a significant impact on sea level fingerprints, especially for sea level change in the near field with estimates of sea level change varying by up to 150% in some regions between 10 km and 100 km resolutions. From future sea level fingerprints based on ice sheet projections under the RCP4.5 and 8.5 scenarios, we conclude that by 2100 each polar ice sheet will have significant contributions to regional sea level distributions. However, for Antarctica, differences in projections between RCP 4.5 and 8.5 lead to different spatial patterns of regional sea level and not just different magnitudes. Finally, by quantifying sea level contributions, we identified the most/least contributing polar ice sheet drainage basins to local sea level rise at

some coastal cities in the 21st century, which may inform public policy and priorities in observations and research. Future studies of sea-level projections will need to consider high-resolution projections of ice mass changes and quantify the contributions of local sea level rise at coastal cities from individual drainage basins of polar ice sheets.

Acknowledgement

First and foremost, I would like to sincerely thank my supervisors, Dr. Xuebin Zhang and Prof. Matt King. I deeply appreciate their invaluable help and instructive guidance throughout this year.

I would like to thank the 2+2 program between Ocean University of China and University of Tasmania. Thanks to IMAS and CSRIO for the help and support.

I would like to express my sincere gratitude to Jinping Wang and Yi Jin, for their kind help and valuable suggestions on both the technical support and academic study in my honours year. My thanks also go to Scott Meyerink for his wonderful proof-reading.

I would like to extend my gratitude to my classmate Meng Han and senior students Xiaoxuan Jiang, Jingwei Zhang and Zeya Li, who have offered me valuable suggestions in both academic studies and the preparation of the thesis.

Last but not least, my thanks would go to my beloved family for their unwavering support and love for the longest time. Thanks for believing and encouraging me during my tough times.

Contents

Abstract	iii
Acknowledgement	v
List of figures	viii
List of tables	x
1. Introduction	11
2. Data and methodology	16
2.1 Sea level theory	16
2.2 ISSM-SESAW module	18
2.3 Data	19
2.3.1 <i>GRACE data</i>	19
2.3.2 <i>1-D elastic Earth models</i>	20
2.3.3 <i>Future projections of polar ice sheets</i>	21
2.3.4 <i>Sea level sensitivity kernel data</i>	24
2.4 Numerical experiment design	26
2.4.1 <i>Validation on ISSM-SESAW computation</i>	26
2.4.2 <i>Resolution test</i>	26
2.4.3 <i>Sensitivity test to 1-D elastic Earth models</i>	27
2.4.4 <i>Future sea level fingerprint computations</i>	28

2.4.5 <i>Kernel-based sea level projections</i>	28
3. Results	30
3.1 Validation of ISSM-SESAW computation.....	30
3.2 Resolution test	34
3.3 Sensitivity test to 1-D elastic Earth models.....	39
3.4 Future sea level fingerprints associated with polar ice sheets melting.....	41
3.5 Kernel-based sea level projections	43
4. Discussions.....	52
4.1 Validation on ISSM-SESAW computation	52
4.2 Resolution test.....	53
4.3 Sensitivity test to 1-D elastic Earth models.....	54
4.4. Future sea level fingerprints in response to projected polar ice sheet mass changes.....	55
4.5 Kernel-based sea level projections	57
4.6 Research limitation and further work	59
5. Conclusions.....	60
References	62

List of figures

Figure 1. Normalized sea level fingerprint (mm) associated with a uniform thinning of the Greenland Ice Sheet (source from: Tamtsiea et al., 2003).

Figure 2. An example of unstructured mesh grids on solid-earth surface for ISSM sea level fingerprint module, in view of the North Pole, with continents depicted in cyan. Mesh along coastlines is fixed in size 50 km. Mesh over GrIS and its near fields is fixed in 100 km. Mesh in continents and open ocean is specified in size with limit range [50, 300] km.

Figure 3. Percentage differences of computed Load Love Numbers (LLNs), h_n , l_n , k_n , between 1-D elastic Earth models PREM, iasp91 and ak135, which are in the center of mass (CM) coordinate system within the degree range of $n \in (1, 10000)$ (reproduced from: Wang et al., 2012). Note that ‘iasp91-PREM’ represents the relative differences of LLNs between iasp91 and PREM 1-D elastic Earth models.

Figure 4. Inferred grounded-ice mass change over the Greenland and Antarctic Ice Sheets from 2000 to 2100 computed under the RCP4.5 and RCP8.5 scenarios (reproduced from: Golledge et al., 2019).

Figure 5. Change in thickness of grounded ice H (m) over the GrIS and AIS in 2100 compared to 2100 under the RCP4.5 and RCP8.5 scenarios (reproduced from: Golledge et al., 2019).

Figure 6. Negative sea level sensitivity kernels $-K_{local}^{\emptyset}$ over the GrIS and AIS for selected coastal cities in near fields (See Fig. 7 for locations of the coastal cities). The negative kernels here refer to positive sensitivity of local sea level change to negative ice thickness change (that is ice melting induces a barystatic sea level rise) (reproduced from: Mitrovica et al., 2018).

Figure 7. Map of 10 selected coastal cities. The numbers are referred to selected cities in Figure. 6 (1- Churchill, Canada, 2- St. Johns, Canada, 3- New York, U.S., 4- Vancouver, Canada, 5- Oslo, Norway, 6-London, U.K., 7-Ushualia, Argentina, 8-Cape Town, South Africa, 9-Perth, Australia, 10- Wellington, New Zealand).

Figure 8. Maps of drainage basins over the Greenland (a) and Antarctic Ice Sheets (b). The numbers in maps of basins are referred to basin ID numbers (Zwally et al., 2012).

Figure 9. Sea level fingerprints computed by ISSM in response to monthly land water storage change from GRACE data for the period April 2002 to August 2016. (a) Linear trends (cm yr⁻¹) in monthly land water storage from GRACE data. (b) Linear trends (mm yr⁻¹) in monthly relative sea level change computed by ISSM. (c) Difference in sea level linear trends between ISSM and spectral methods (ISSM minus spectral method).

Figure 10. Validation of normalized sea level fingerprints computed by ISSM associated with a uniform thinning of the GrIS (a, b) and AIS (c, d). Panel (a) and (c) show normalized sea level fingerprints computed by ISSM under the GrIS and AIS uniform melting scenarios,

respectively. Panel (b) and (d) show difference in normalized sea level fingerprints between ISSM and spectral methods (ISSM minus spectral method).

Figure 11. Difference in normalized sea level fingerprints of different resolutions (5 km, 10 km, 25 km, 50 km, 100 km) for the GrIS (a, b, c, d) and AIS (e, f, g, h) domains, in response to high-resolution projected ice thickness change over individual ice sheets (GrIS-2.5 km, AIS-5 km) in 2100 compared to 2000 under the RCP8.5 scenario. Each caption indicates the comparison of fingerprints between two resolutions.

Figure 12. Comparisons of normalized sea level fingerprints computed with PREM, iak135 and iasp91 1-D elastic Earth models, in response to uniform thinning of the GrIS (a, b, c) and AIS (d, e, f). Panel (a) and (d) show normalized sea level changes computed on PREM Earth model. Panel (b) and (e) show difference in normalized sea level fingerprints between PREM and iak135 Earth models for the GrIS and AIS melting scenarios, respectively. Panel (c) and (f) show difference in normalized sea level fingerprints between PREM and iasp91 Earth models for the GrIS and AIS melting scenarios, respectively.

Figure 13. Linear trends in future sea level fingerprints (mm yr^{-1}) associated with individual polar ice sheets melting during the period 2000-2100 under the RCP4.5 (a-GrIS, c-AIS) and 8.5 (b-GrIS, d-AIS) scenarios. The barystatic sea level trend (mm yr^{-1}) under each melting scenario in the 21st century is shown on top of each panel.

Figure 14. Maps of the GrIS drainage basins (a) and the selected cities (b). The numbers in the basin map (a) are referred to as basin ID numbers (Zwally et al., 2012). The numbers in the city map (b) are referred to the selected cities in Fig. 15 (1- Churchill, Canada, 2- St. Johns, Canada, 3- New York, U.S., 4- Vancouver, Canada, 5- Oslo, Norway, 6- London, U.K., 7- Ushualia, Argentina, 8- Cape Town, South Africa, 9- Perth, Australia, 10- Wellington, New Zealand).

Figure 15. Future kernel-based projection of sea level in the 21st century for each of 19 drainage basins of the GrIS (see Fig. 14a for GrIS drainage basin definition). Panel (a) presents the area-averaged ice thickness changed in 2100 compared to 2000 under the RCP4.5 and RCP8.5 scenarios. Panel (b) presents the local sea level changed for selected coastal cities due to uniform one-meter ice thickness reduction over each GrIS basin (see Fig. 14b for coastal city locations). Panels (c) and (d) present kernel-projected contributions to local sea level for the selected coastal cities in the 21st century under RCP4.5 and RCP8.5, respectively.

Figure 16. Maps of the AIS drainage basins (a) and the selected cities (b). The numbers in the basin map (a) are referred to as basin ID numbers (Zwally et al., 2012). The numbers in the city map (b) are referred to the selected cities in Fig. 17 (1- Churchill, Canada, 2- St. Johns, Canada, 3- New York, U.S., 4- Vancouver, Canada, 5- Oslo, Norway, 6- London, U.K., 7- Ushualia, Argentina, 8- Cape Town, South Africa, 9- Perth, Australia, 10- Wellington, New Zealand).

Figure 17. Future kernel-based projection of sea level in the 21st century for 27 drainage basins of the AIS (see Fig. 16a for AIS drainage basin definition). Panel (a) presents the area-averaged

ice thickness changed in 2100 compared to 2000 under the RCP4.5 and RCP8.5 scenarios. Panel (b) presents the local sea level changed for the selected coastal cities due to a uniform one-meter ice reduction over each of the AIS basins (see Fig. 16b for coastal city locations). Panels (c) and (d) present kernel-projected contributions to local sea level for the selected coastal cities in the 21st century, under RCP4.5 and 8.5, respectively.

List of tables

Table 1. Computation resources of ten ISSM meshes used in resolution test, including numbers of vertices, elements of ISSM mesh and computation time.

1. Introduction

Sea level rise, mainly due to thermal expansion of ocean water and melting of land ice, is one of the most alarming indicators of anthropogenic climate change. During the 21st century and beyond, sea level change is very likely to be strongly non-uniform, with significant deviations of regional sea level from the global mean sea level (Church et al., 2013). It is projected that by the end of the 21st century, 70% of global coastlines will experience regional sea level deviations of up to 20% of the global mean sea level rise (Church et al., 2013). The deviations in regional sea-level change can be caused by several physical processes, such as ocean density and circulation change, loss of mass from land ice (including Greenland Ice Sheet (GrIS), Antarctic Ice Sheet (AIS), Glacier and Ice Caps (GIC)), terrestrial water storage change, and glacial isostatic adjustment (GIA) (Church et al., 2013).

The regional sea level distribution associated with contemporary melting of land ice (i.e. melt events span from decades to one century), have been referred to as sea level fingerprints (Clark and Lingle, 1977, Conrad and Hager, 1997, Mitrovica et al., 2001, Tamisiea et al., 2001, Plag, 2006, Gomez et al., 2010, Mitrovica et al., 2011). An example for the sea level fingerprint due to a uniform thinning of the GrIS is shown in Fig.1 (Tamtsiea et al., 2003), with normalized sea level changes shown (i.e., uniform melt of GrIS of equivalent of 1 mm of global-mean sea level would produce the pattern in Fig. 1 and with units of mm). These patterns only represent the static sea level change and do not include other sea-level influences such as ocean dynamics. The sea level fingerprint indicates that the uniform thinning of the GrIS induces non-uniform sea level distributions, with a sea level fall in the near field and a greater than barystatic sea level rise (i.e., global-mean sea level due to addition of water mass to ocean) in the far field. As the fingerprints are effectively the same for the same spatial distribution of land ice mass change, the pattern in Fig. 1 would be maintained with large or small uniform melting of GrIS but with different magnitudes.

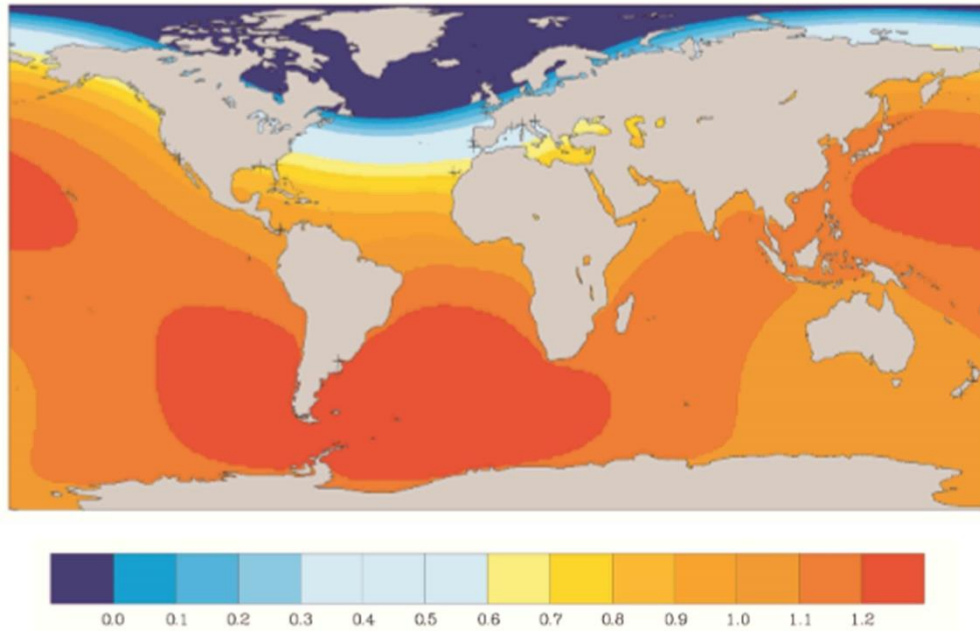


Figure 1. Normalized sea level fingerprint (mm) associated with a uniform thinning of the Greenland Ice Sheet (source from: Tamtsiea et al., 2003).

The sea level fingerprints due to contemporary mass distribution are calculated following a governing sea level equation, in which the effects of gravitation, solid-earth deformation, and rotation are all considered (Riva et al., 2017, Quinn et al., 2015, Mitrovica et al., 2011, Milne et al., 1999, Farrell and Clark, 1976). One classical numerical method to solve the sea level equation is the Green's function approach. This approach exploits discs of various sizes and distances from the observation point with the Green's function to yield the spatial convolution of the surface loads (Farrell and Clark, 1976, Clark and Lingle, 1977, Clark et al., 1978). However, due to non-uniform distributed discs, the global surface loads in this approach was caused in space-domain discretization, which leading to non-uniform resolutions in sea level calculations (Mitrovica et al., 2011). Currently, the sea level fingerprints are most widely computed using spectral methods (e.g., either fully spectral solver or pseudo-spectral solver) (Mitrovica and Peltier, 1991, Johnston, 1993, Milne and Mitrovica, 1998, Milne et al., 1999, Kendall et al., 2005). These methods avoided the space-domain discretization in the Green's function approach by changing the expressions of surface load changed into spherical harmonics forms (Mitrovica et al., 2011). However, these numerical methods usually have difficulty resolving high-resolution surface loads and providing high-resolution sea level

fingerprints due to high computational cost and potential numerical instability (Adhikari et al., 2016).

In numerical computations, the perturbations in gravity fields, solid-earth deformation by contemporary mass redistributions depends on the Earth crustal structures in the Earth models. Although there exists substantial 3-D (lateral and radial) variations in Earth crustal structures, 1-D (i.e., radially varying) elastic Earth models are commonly adopted for simplification. In each 1-D elastic Earth model the crustal structures are embedded within the load Love numbers (LLNs) h_n , k_n , l_n . These numbers are generally adopted to express the load Green's functions (LGFs) as the surface deformation of the 1-D elastic Earth model due to a point load on the Earth's surface. However, the computed LLNs (e.g., ~up to 60% difference of l_n) and LGFs (e.g., ~up to 26% difference of radial displacement) are significantly different in various 1-D elastic Earth models, including PREM (Dziewonski and Anderson, 1981), iasp91 (Kennett and Engdahl, 1991) and ak135 (Kennett et al., 1995) Earth models (Wang et al., 2012). These differences among the Earth models will likely result in difference in sea level fingerprints in response to land ice mass changes. So far, no studies have investigated this uncertainty in sea level fingerprints due to different 1-D elastic Earth models.

In forward computation of sea level fingerprints, it is easy to yield regional sea level change in response to contemporary land ice mass variations. But a big question for local stakeholders at coastal cities is to identify the most contributing ice sources to their local sea levels in the future. To address this problem, some recent studies attempted to apply sea level fingerprints to the investigations for the site-specific sea level sensitivity kernel for major coastal cities to the land ice mass changes (Larour et al., 2017, Mitrovica et al., 2018). Like inverse modelling, the sea level sensitivity kernel quantifies the relationship between local sea level change at a specific city of interest to ice thickness changes over any ice location. Incorporated with realistic ice melt scenarios, the kernel sensitivity method provides a powerful tool (called 'kernel-based sea level projection') for coastal planners to make local sea level projection by calculating local sea level contributions (Mitrovica et al., 2018). However, there are few studies using this

method to quantify future sea level contributions for coastal cities by projected mass changes over polar ice sheets (Larour et al., 2017, Mitrovica et al., 2018). This limits the ability of local governments to make accurate future local sea level projections and provide efficient guidance to develop sound mitigation and adaptation strategies.

Previous studies of the contribution of changing ice sheets on local sea level changes using sensitivity kernel method focused on large-scale ice sheet change such as all of the GrIS, WAIS or EAIS (e.g., Larour et al., 2017). But ice mass over the entire ice sheet normally does not change uniformly (Bolch et al., 2013, Rignot et al., 2019, Schröder et al., 2019, Shepherd et al., 2019). For example, more ice mass loss was observed by recent altimetry in northwest and southeast drainage GrIS basins than in other basins (Smith et al., 2020). It means ice melting in different locations within the same ice sheets may lead to various sea level contributions. Therefore, it is required to quantify local sea level contributions of ice mass change in smaller areas, such as individual ice drainage basins instead of the whole ice sheets to coastal cities. Basin-quantified sea level contribution is critical for coastal planners and policymakers to guide future observations of the evolution of land ice geometries at drainage basin level.

In this research, our goal is to provide high-resolution sea level projections in response to future land ice mass changes over polar ice sheets in the 21st century as a guide to local stakeholders for better mitigation strategies and scientific observations. To this aim, we utilize the unstructured mesh-grid sea level fingerprint module - ISSM's Solid Earth and Sea level Adjustment Workbench (ISSM-SESAW), developed by NASA/Jet Propulsion Laboratory (JPL) to compute high-resolution sea level fingerprints by exploiting Green's functions of high-resolution ice mass changes on refined unstructured mesh grids to solve the sea level equation in a rotating, 1-D elastic Earth model. The unstructured mesh-grid system greatly enhances the ability of the module to resolve fine structures of both melting sources and target coasts in kilometer-scale resolution with great accuracy (Wessel et al., 2013, Adhikari et al., 2016). This module is computationally efficient as it allows users to control the number of elements of

mesh grids without losing high-resolution information at locations of interest or importance (e.g., fast-flowing outlet glaciers, coastlines of interest) (Adhikari et al., 2016).

In this study, based on ISSM-SESAW, we provide high-resolution sea level fingerprints in response to future ice thickness change over polar ice sheets in the 21st century under the Representative Concentration Pathway (RCP) 4.5 and 8.5 scenarios. We test the sensitivities of the sea level fingerprints to different spatial resolutions of melting ice sheets and the choice of 1-D elastic Earth models. Furthermore, we make local sea level projections at some representative coastal cities by quantifying sea level contributions over the 21st century from individual ice sheet drainage basins.

This thesis is divided into five sections. Besides this section, section 2 introduces data and methodology. Section 3 shows the main results. Specifically, section 3.1 validates the sea level fingerprints computed by ISSM-SESAW; Section 3.2 presents the comparison of fingerprints computed on different resolutions over polar ice sheets in the mesh-grid system of ISSM-SESAW; Section 3.3 tests the sensitivity of sea level fingerprints to various 1-D elastic Earth models; Section 3.4 provides high-resolution sea level fingerprints associated with future ice mass changes over polar ice sheets and section 3.5 quantifies the sea level contributions to some coastal cities by individual drainage basins over polar ice sheets. Finally, the discussions and conclusions are given in sections 4 and 5, respectively.

2. Data and methodology

2.1 Sea level theory

Regional sea level distribution associated with the melting of ice sheets was firstly recognized by Woodward in 1888. Woodward (1888) assumed a non-rotating, rigid earth and considered the self-gravitation of the surface load (ice and water) was the only contributor to the geographically variable patterns in sea level change following an ice sheet melting. After almost one century, Farrell and Clark (1976), who, based on previous discussion of Earth's deformation, combined the Earth's elastic-viscous effect and gravitational effect on sea level change in response to land ice melting into a gravitationally self-consistent sea level theory. In this theory, Farrell and Clark adopted a non-rotating but deformable Earth model with a fixed shoreline geometry. The effects of shoreline migration (Lambeck and Nakada, 1990, Johnston, 1993, Peltier, 1994) and perturbations in rotation vector (Milne and Mitrovica, 1998) have subsequently been added to the theory. Milne et al. (1999) combined these two additional effects into a new extended version of sea level equation as follows:

$$S(\theta, \psi, t) = N(\theta, \psi, t) - U(\theta, \psi, t), \quad (1)$$

where the change in relative sea level $S(\theta, \psi, t)$ is defined as the change in height of sea surface $N(\theta, \psi, t)$ subtracted by the change in height of solid surface $U(\theta, \psi, t)$. (θ, ψ) are spatial coordinates that represent latitude and longitude, and t is time. The Earth's rotational effects, gravitational effects and Earth's elastic response are included in two boundary functions: $N(\theta, \psi, t)$ and $U(\theta, \psi, t)$.

Next, we will separately give the mathematical descriptions of two boundary functions following several previous studies (e.g., Tamisiea et al., 2001, Gomez et al., 2010, Adhikari et al., 2016). Change in sea surface $N(\theta, \psi, t)$ is a linear function of perturbations in gravitational potential Φ and rotational potential Λ , and other terms as follows:

$$N(\theta, \psi, t) = \frac{1}{g} [\Phi(\theta, \psi, t) + \Lambda(\theta, \psi, t)] + E(t) + C(t), \quad (2)$$

where g is the gravitational acceleration, E is the barystatic sea level change and C is the global mean of spatial gravitational potential changes (Φ) and solid earth deformations (Λ). E and C are both barystatic terms to satisfy the mass conservation constraint (Farrell and Clark, 1976).

The radial displacement of solid surface U is the combination of Earth's elastic response due to perturbations in gravitational potential U_Φ and solid surface deformation by changes in rotational potential U_Λ as follows:

$$U(\theta, \psi, t) = U_\Phi(\theta, \psi, t) + U_\Lambda(\theta, \psi, t). \quad (3)$$

To compute perturbations in gravitational potentials Φ and rotational potentials Λ as well as associated deformations in Earth's solid surface U_Φ and U_Λ , it requires a global mass-conserving load function as follows (Farrell and Clark, 1976, Mitrovica and Peltier, 1991, Konrad et al., 2015, Adhikari et al., 2016, Mitrovica et al., 2018),

$$L(\theta, \psi, t) = \rho_l H(\theta, \psi, t) + \rho_o S(\theta, \psi, t) O(\theta, \psi), \quad (4)$$

where $H(\theta, \psi, t)$ is the change in land ice thickness in time period t , and $S(\theta, \psi, t)$ is the same relative sea level change in Eq. 1. $O(\theta, \psi)$ is the ocean function (Munk and Macdonald, 1960). By definition, $O = 1$ for oceans and $O = 0$ otherwise. This load function L can be directly used to compute perturbations in gravitational potential Φ and associated deformations in Earth's solid surface U_Φ by convolving with respective Green's functions. According to the Eulerian theory of rotation, mass redistributions on Earth's surface would perturb the rotating axis of the Earth and lead to changes in global rotational potentials and associated solid surface deformations (Dahlen, 1976, Wahr, 1985, Lambeck, 1988). Therefore, in the sea level theory the perturbations in rotational potential Λ and associated deformations in Earth's solid surface U_Λ driven by land ice mass variations can also be determined from the load function L .

Governed by the sea level theory, the relative sea level change is linearly related to the ice load (Farrell and Clark, 1976). Therefore, the local sea level change at one site in response to contemporary ice mass redistributions can be also expressed in the following form,

$$S_{\text{local}} = \int H(\theta, \psi) K_{\text{local}}^{\theta}(\theta, \psi) dA, \quad (5)$$

where S_{local} is the relative sea level change at one site (in mm), *local* refers to one specific site (e.g., London), (θ, ψ) represents the same spatial coordinates in Eq. 1 and H is ice thickness change (in m). $K_{\text{local}}^{\theta}$ is sensitivity kernel, which reflects the change in local relative sea level in response to a prescribed ice thickness change over an ice domain of given area (in mm per m per m^2). dA is the area of ice domains (in m^2). This expression is very useful for local sea level projections since it can be applied to any land ice domains to calculate its sea level contribution to coastal cities.

2.2 ISSM-SESAW module

In this research we adopted the unstructured mesh-grid sea level fingerprint module - ISSM-SESAW developed by NASA/JPL to exploit Green's functions on the mesh-grid system to solve the sea level equation and provide high-resolution sea level fingerprints.

In ISSM-SESAW fingerprints computations, the simulation of all variables in the sea level equation is based on the unstructured mesh-grid system. The unstructured mesh is generated using Gmsh (Geuzaine and Remacle, 2009). Each element of mesh grid has a different size, which is a consequence of anisotropic mesh refinement based on the Bidimensional Anisotropic Mesh Generator (BAMG) package developed by Hecht (2006). The anisotropic mesh architecture allows users to control the number of elements of the mesh grids without losing high-resolution fingerprints at locations of interest (e.g., fast-flowing outlet glaciers, coastal cities for planning), which greatly enhances the module's computational efficiency (Adhikari et al., 2016). An example of the refined anisotropic mesh on the solid-Earth surface is shown in Fig. 2, which consists of 19535 vertices and 39066 elements.

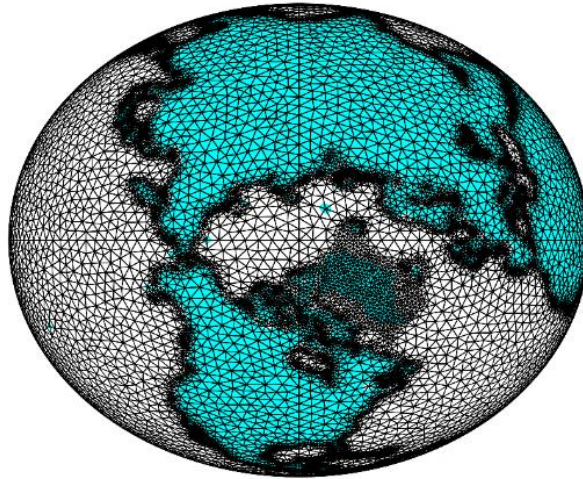


Figure 2. An example of unstructured mesh grids on solid-earth surface for ISSM sea level fingerprint module, in view of the North Pole, with continents depicted in cyan. Mesh along coastlines is fixed in size 50 km. Mesh over GrIS and its near fields is fixed in 100 km. Mesh in continents and open ocean is specified in size with limit range [50, 300] km.

However, the validity of sea level fingerprints computed by ISSM-SESAW module are limited on timescales within about one century, because the ISSM-SESAW module was based on a simplified 1-D elastically compressible and self-gravitating Earth model. The approximation of elastic deformation of the solid Earth is only valid from mass changes within timescales from decades to one century, with the exception of a few regions globally underlain by low viscosity mantle (Adhikari et al., 2016). Therefore, we only consider the case for sea level response to contemporary and near-future melting of land ice (i.e., melting from decades to one century).

2.3 Data

2.3.1 GRACE data

In recent decades, the twin Gravity Recovery and Climate Experiment (GRACE) satellites provide a real-time way to monitor and measure the monthly time-varying Earth's gravity field

(Wouters et al., 2014). Based on GRACE Level-2 Release-06 data products from JPL processing center, Adhikari et al. (2019) provided the monthly land water height anomalies data from March 2002 to June 2016 (denoted as the ‘GRACE period’). The data was inferred from the gravity variations driven by land water storage in the GRACE period with reference to the 11-year (January 2003-December 2013) mean values and corrected for GIA effect. Here, we used $0.5^{\circ} \times 0.5^{\circ}$ gridded monthly land water height anomalies data from the GRACE period from Adhikari et al. (2019) to calculate sea level fingerprints driven by the contemporary land ice mass changes during this period.

2.3.2 1-D elastic Earth models

A 1-D elastic Earth model describes the solid Earth with elastic Earth parameters (e.g., P-wave velocity, S-wave velocity and density) which determine different rheology properties in radially varying layers. In this study, three 1-D elastic Earth models were compared: PREM (Dziewonski and Anderson, 1981), iasp91 (Kennett and Engdahl, 1991) and ak135 (Kennett et al., 1995). PREM Earth model was established using the data of body wave travel times and periods of normal modes collected from year 1964 to 1975 (Dziewonski and Anderson, 1981), while the data of body waves used for iasp91 (Kennett and Engdahl, 1991) and ak135 (Kennett et al., 1995) Earth models were extended to 1987 and 1991, respectively. PREM is the most widely used elastic Earth model for studies of this kind.

The radially varying crustal structure in each 1-D elastic Earth model is embedded within the LLNs, h_n , k_n , l_n which are used to express LGFs as surface deformation of the Earth model due to a point load on the Earth’s surface. In this study, we adopted the computed LLNs numbers in the center of mass (CM) coordinate system within the degree range of $n \in (1, 10000)$ for the 1-D elastic Earth models (i.e., PREM and iasp91 and ak135) provided by Wang et al. (2012).

Figure 3 shows the percentage differences of LLNs between pairs of the adopted Earth models (iasp91 and PREM, ak135 and PREM, ak135 and iasp91). There is no significant difference

(<10%) in LLNs between ak135 and iasp91. But the comparison with PREM and any of the other two models shows there are large differences for degrees around 200 (~14% for h_n , ~60% for l_n , ~20% for k_n) and degrees above 1000 (~12% for h_n).

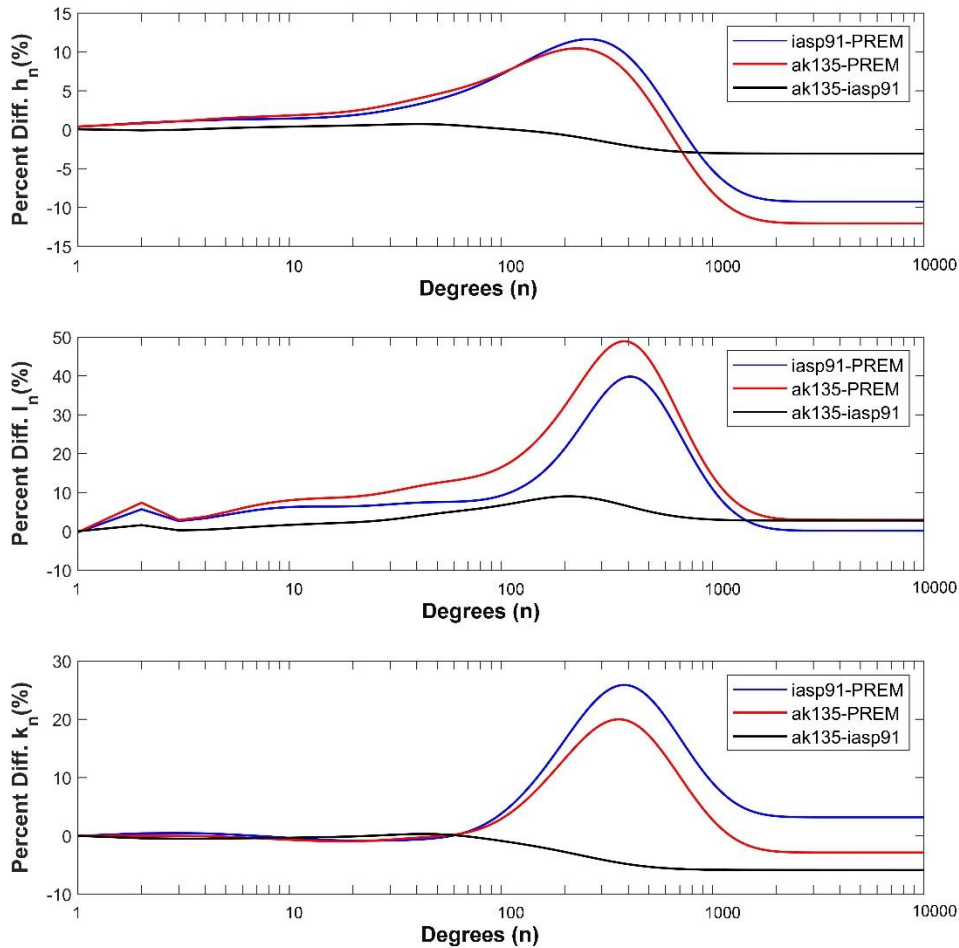


Figure 3. Percentage differences of computed Load Love Numbers (LLNs), h_n , l_n , k_n , between 1-D elastic Earth models PREM, iasp91 and ak135, which are in the center of mass (CM) coordinate system within the degree range of $n \in (1, 10000)$ (reproduced from: Wang et al., 2012). Note that ‘iasp91-PREM’ represents the relative differences of LLNs between iasp91 and PREM 1-D elastic Earth models.

2.3.3 Future projections of polar ice sheets

For this study, we used high-resolution projections of polar ice geometries over the GrIS and AIS at 5-year increments for the period 2000-2100 computed under the RCP 4.5 and 8.5 scenarios (Golledge et al., 2019). The geometry dataset contains geographic variations of ice thickness, ice surface elevation and bedrock elevation for all areas over the GrIS and AIS at horizontal resolutions of 2.5 km and 5 km, respectively. The geometry variations were simulated by the Parallel Ice Sheet Model (PISM) coupled with intermediate-complexity climate model using sub-grid-scale grounding-line parameterizations (Golledge et al., 2019). The geometry data computed with (i.e., forced run) or without (i.e., control run) ice-sheet meltwater feedback were both provided.

To derive the thickness data associated with sea level contribution from the geometry dataset, we performed the following steps. Firstly, we collected the grounded-ice geometry data, excluding floating ice as it does not contribute to sea level change beyond negligible steric effects. Secondly, we used a hydrostatic calculation to derive thickness data of the grounded ice that is above the hydrostatic equilibrium, since the grounded ice that is below the equilibrium does not contribute to sea level either.

We then corrected for model bias by comparing and removing the ice thickness change data from the control run from the forced run. For convenience, the bias-corrected forced-run thickness change and its inferred mass change are denoted as thickness change data and mass change data.

The temporally varied mass changes over the whole grounded-ice areas in the GrIS and AIS from 2000 to 2100 under the RCP4.5 and RCP8.5 scenarios are shown in Fig. 4. The spatial distribution of thickness change in grounded ice across the GrIS and AIS in 2100 relative to 2000 under RCP4.5 and RCP8.5 is shown in Fig. 5.

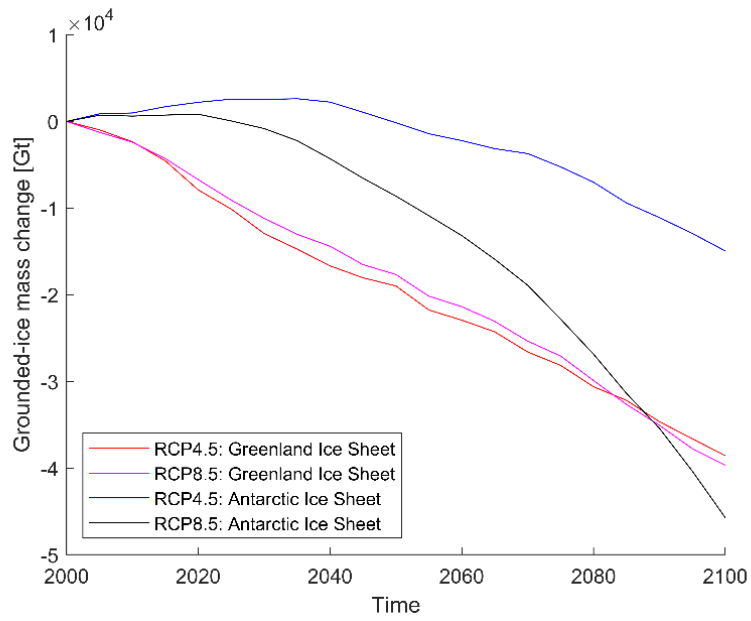


Figure 4. Inferred grounded-ice mass change over the Greenland and Antarctic Ice Sheets from 2000 to 2100 computed under the RCP4.5 and RCP8.5 scenarios (reproduced from: Golledge et al., 2019).

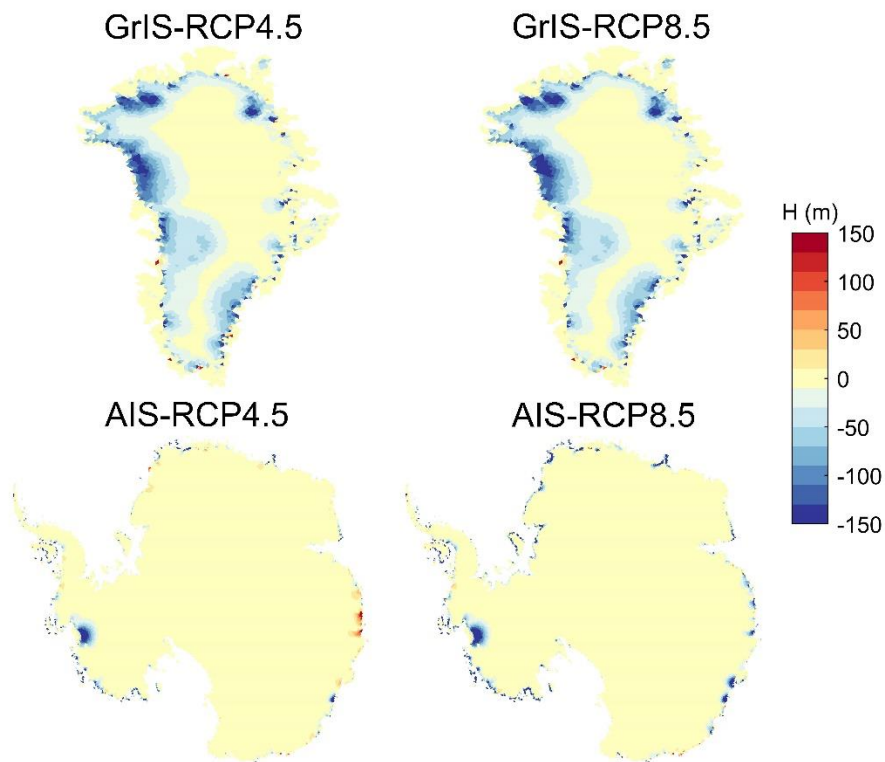


Figure 5. Change in thickness of grounded ice H (m) over the GrIS and AIS in 2100 compared to 2100 under the RCP4.5 and RCP8.5 scenarios (reproduced from: Golledge et al., 2019).

2.3.4 Sea level sensitivity kernel data

Sea level sensitivity represents the sensitivity of local sea level to ice thickness change over ice domains. It can be derived using different methods, such as gradient fingerprint mapping from an adjoint method (Larour et al., 2017) and sea level sensitivity kernel from numerical fingerprint computations (Mitrovica et al., 2018).

Here, we adopted the sea level sensitivity kernel dataset from Mitrovica et al. (2018), which were computed for ~ 740 tide gauge sites to ice thickness over areas across GrIS and AIS (<https://doi.org/10.5281/zenodo.1170110>). The site-specific kernels in the database are given at Gauss-Legendre points, with 512 latitudes and 1024 longitudes for GrIS kernels and 256 latitude and 512 longitudes for AIS kernels. Here, we transformed the Gauss-Legendre points to latitude and longitude grids ($\sim 0.35^\circ \times 0.35^\circ$ grid for GrIS kernels and $\sim 0.7^\circ \times 0.7^\circ$ grid for AIS kernels) used for integration in Eq.5, using the functions provided by Holt (2020). We also changed the spherical kernels in the dataset to new kernels K_{local}^\emptyset in Eq. 5 which physically represents the change in local relative sea level (per mm) induced by unit ice thickness change (in m) occurring over unit ice domain areas (in m^2).

The negative sea level sensitivity kernels $-K_{local}^\emptyset$ over the GrIS and AIS for selected coastal cities are shown in Fig. 6, which represents the change in local relative sea level (per mm) induced by unit ice thickness reduction (in m) occurring over unit ice domain areas (in m^2). It shows the sensitivity of local sea level change to negative ice thickness change (i.e., ice thickness reduction). For example, the kernel of St Johns to the GrIS (shown in Fig. 6) indicates that the ice loss in the northern GrIS contributes to rising sea level at St Johns but the southern GrIS melting would induce a falling in sea level at St Johns. The spatial gradients in kernels reflect differences in sea level sensitivities of coastal cities to melting over ice locations. For example, the kernel of Perth to the AIS (shown in Fig. 6) shows that local sea level rise at Perth is more sensitive to melting in the WAIS than the EAIS.

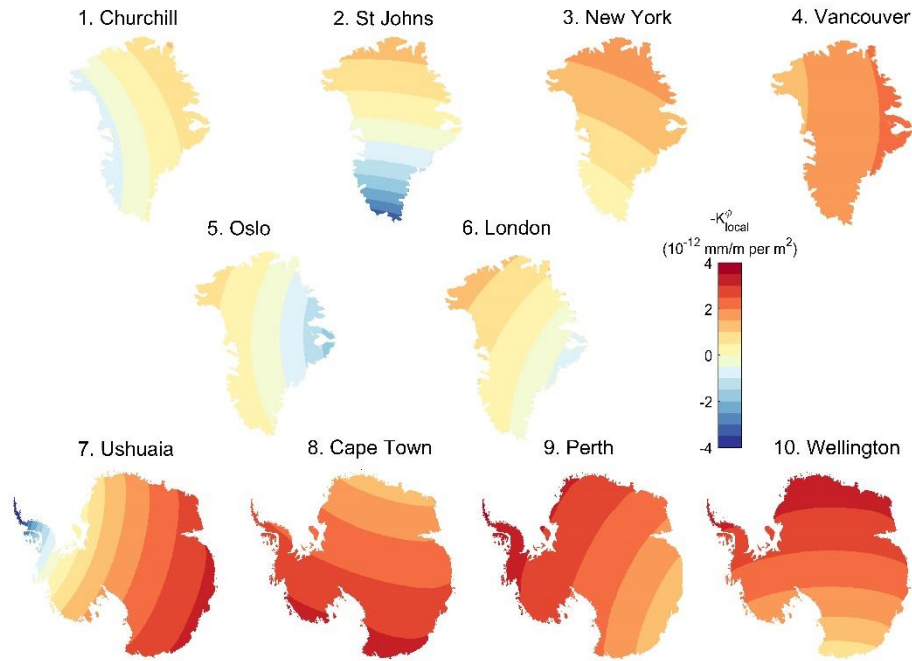


Figure 6. Negative sea level sensitivity kernels $-K_{local}^0$ over the GrIS and AIS for selected coastal cities in near fields (See Fig. 7 for locations of the coastal cities). The negative kernels here refer to positive sensitivity of local sea level change to negative ice thickness change (that is ice melting induces a barystatic sea level rise) (reproduced from: Mitrovica et al., 2018).

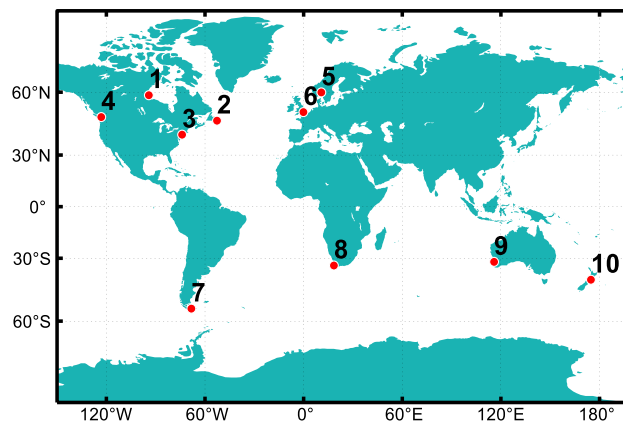


Figure 7. Map of 10 selected coastal cities. The numbers are referred to selected cities in Figure. 6 (1- Churchill, Canada, 2- St. Johns, Canada, 3- New York, U.S., 4- Vancouver, Canada, 5- Oslo, Norway, 6- London, U.K., 7-Ushualia, Argentina, 8-Cape Town, South Africa, 9-Perth, Australia, 10- Wellington, New Zealand).

2.4 Numerical experiment design

2.4.1 Validation on ISSM-SESAW computation

Despite the difference in numerical methods, the sea level fingerprints due to contemporary mass redistribution on the Earth surface are basically determined by the same governing sea level equation (refer to section 2.1). Therefore, sea level fingerprints computed by ISSM-SESAW and other methods should be comparable. To verify this, we performed two validation experiments by comparing sea level fingerprints computed by ISSM-SESAW and other numerical methods to check the reliability of solutions by ISSM-SESAW. Firstly, we used ISSM-SESAW to compute sea level fingerprints in response to monthly land water storage change for the period March 2002 to Jun 2016 derived from GRACE satellite data (Adhikari et al., 2019). Fingerprints were computed at 300 km resolution. To compare with published fingerprints based on the spectral method using the same melting scenarios (Adhikari et al., 2019), we computed a linear trend through the monthly fingerprints. The comparison of two fingerprints and changes in land water storage from GRACE data are shown in Fig. 9 in section 3.1.

Secondly, we used ISSM-SESAW to compute sea level fingerprints in response to the uniform melting scenarios (i.e., ice thickness over the whole GrIS or AIS was reduced uniformly). Fingerprints were computed at 40 km resolution. Then we normalized the fingerprints by the barystatic sea level change. The comparable fingerprints simulated from the same melting scenarios were computed using spectral methods by Mitrovica et al. (2001). The comparisons of fingerprints due to uniform melting over the whole GrIS and AIS are shown in Fig. 10 in section 3.1.

2.4.2 Resolution test

Spectral methods are widely used to compute contemporary sea level fingerprints, but the simulations are usually limited to coarse resolutions, e.g., on the order of $\sim 1^\circ$ (Adhikari et al.,

2016). Consequently, errors in sea level fingerprints might arise due to the limitation in capturing fine structure near melting sources. We aimed to find the optimal resolutions of these simulations by testing the sensitivity of sea level fingerprints to different resolutions of ice melting sources.

To this aim, we designed 10 ISSM meshes using the same resolutions in most areas (50 km for coastlines, 300 km for open oceans and continental lands), except for five meshes with resolutions over the GrIS at 100 km, 50 km, 25 km, 10 km, and 5 km resolutions, respectively, and the other five meshes with resolutions over the AIS at 100 km, 50 km, 25 km, 10 km, and 5 km resolutions, respectively. Then we interpolated high-resolution ice thickness change data over the GrIS (2.5 km) onto each of the former five meshes and compared the computed fingerprints. Similarly, we interpolated high-resolution thickness change data over the AIS (5 km) onto each of the latter five meshes and compared the computed fingerprints. The comparisons of computed sea level fingerprints on different ISSM meshes are shown in Fig. 11 and discussed in section 3.2. Finally, we selected one ISSM mesh with capability to provide the optimal fingerprints with relatively less computational requirement for use in future sea level fingerprint computations.

2.4.3 Sensitivity test to 1-D elastic Earth models

1-D elastic Earth model is characterized by its unique radially varying layers in the Earth's crustal structures. The distinction in these crustal structures between various 1-D elastic Earth models may lead to different responses in sea level fingerprints. In this study, one of the aims is to test the impacts on sea level fingerprints caused by adopting different 1-D elastic Earth models. We chose three 1-D elastic Earth models, namely PREM, iasp91 and ak135 (refer to section 2.3.2), for our testing. For each Earth model, we employed the computed LLNs in the center of mass (CM) coordinate system and lies in the range of $n \in (1, 10000)$ from Wang et al. (2012). Then we adopted each 1-D elastic Earth model in ISSM-SESAW module to perform sea level fingerprints in response to the uniform melting scenarios (i.e., ice thickness over the

GrIS and AIS was uniformly reduced by one meter). By comparing the difference in sea level fingerprints between pairs of the Earth models, the sensitivity of sea level fingerprints to different 1-D elastic Earth models is derived (Fig. 12) and discussed in section 3.3.

2.4.4 Future sea level fingerprint computations

In this study, we aimed to use the ISSM-SESAW module to provide high-resolution future sea level fingerprints in response to high-resolution projected polar ice sheet mass variations over the GrIS and AIS by end of the 21st century. For this purpose, we run ISSM-SESAW module forced by thickness data at 5-year increments from 2000 to 2100 under the RCP4.5 and RCP8.5 scenarios (Golledge et al., 2019). We re-gridded ice thickness data at 5-year interval from 2000 to 2100 onto the ISSM mesh to calculate sea level fingerprints. To capture fine structures from melting sources and save much computation costs, we picked up the optimal ISSM mesh based on the resolution tests described in section 2.4.2. Finally, by taking a linear trend of sea level fingerprints computed at 5-year increments from 2000 to 2100, we derived the trends in sea level change during the 21st century due to land ice mass changes from the GrIS and AIS under RCP4.5 and RCP8.5.

2.4.5 Kernel-based sea level projections

To find the most contributing drainage basins in the GrIS and AIS to local sea level at coastal cities by the end of 21st century, we adopted kernel-based sea level projection, a powerful method to calculate sea level contributions from individual polar ice sheet basins for some major coastal cities (Mitrovica et al., 2018). Based on these quantified sea level contributions, more specific guidance for future scientific research into certain basins could be identified for the interests of local communities.

According to Eq. 5, we projected the sea level contributions by combining site-specific kernels and future ice thickness projections. In this experiment, the ice thickness change H is the projected thickness change data in 2100 relative to 2000 by Golledge et al. (2019) (refer to section 2.3.3) and the site-specific kernels K_{local}^{\emptyset} are provided by Mitrovica et al. (2018) (refer to section 2.3.4). Here, we chose ten representative coastal cities for local sea-level projection (see Fig. 7 for location of the selected cities). Firstly, we re-gridded future ice thickness change H to kernel grids in latitudes and longitudes. Then according to the Eq. 5, we multiplied kernels K_{local}^{\emptyset} and future ice thickness change H on kernel grids and integrated them on grids over areas dA for individual polar ice sheet drainage basins (see Fig. 8 for location of the drainage basins). By integrating over each individual drainage basin, we projected contributions to local sea level change at the selected coastal cities by each polar ice sheet basin during the 21st century.

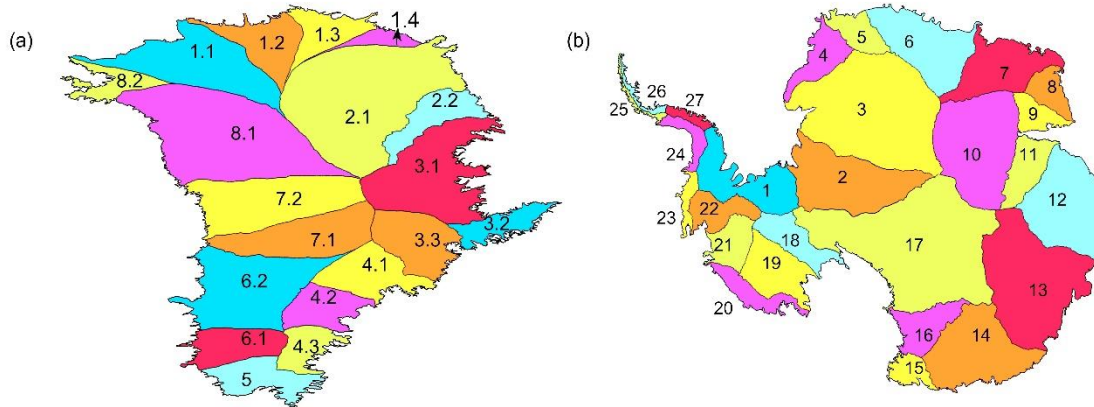


Figure 8. Maps of drainage basins over the Greenland (a) and Antarctic Ice Sheets (b). The numbers in maps of basins are referred to basin ID numbers (Zwally et al., 2012).

3. Results

3.1 Validation of ISSM-SESAW computation

To validate ISSM-SESAW computation, we compared sea level fingerprints computed using ISSM in our study and those using spectral methods in other published papers. The first comparison involves the computation of sea level fingerprints associated with land water storage change from GRACE data over April 2002 to August 2016 (Fig. 9). The second comparison involves the computation of sea level fingerprints, normalized by the barystatic sea level change, for a uniform thinning of each of the GrIS and AIS (Fig. 10).

Using monthly land water storage change for the period April 2002 to August 2016 from GRACE data, we derived associated monthly relative sea level change by ISSM. Then we derived a linear trend over the period and compared it to the trend derived by Adhikari et al. (2019), who computed the sea level fingerprints using spectral methods (Fig. 9).

Over the GRACE period, substantial ice loss (dark blue shading) is evident over the whole GrIS, margins of the WAIS and some glacier systems (e.g., Alaska) (Fig. 9a). Moderate ice growth (dark red shading) is present along part of coasts of the EAIS. Smaller land water storage change (light blue and red shading) is found in other continent regions due to local hydrology processes.

Driven by those mass changes, there are resultant relative sea level change due to the effect of gravitational and rotational changes as well as solid earth response to the surface loading. Sea level fingerprint solution by ISSM indicates significant sea level falls in the near fields of the GrIS and WAIS (dark blue) and a gradual shift towards positive sea level rise (blue to yellow to red) for sites further from the regions (Fig. 9b). It is associated with the changes in the gravity field and rotational potentials driven by the substantial ice loss of the GrIS and WAIS, which causes an overall relative sea level falling and rising in the near and far fields, respectively. In contrast, there is an evident sea level rise (red) in near fields of coastlines of EAIS and a shift

to a lower sea level rise (orange) at further distances due to the moderate ice growth at the EAIS coasts.

Both ISSM and spectral methods give similar solutions, as indicated by small differences in linear trends of the sea level fingerprints between the two methods (Fig. 9c). ISSM computation gives a higher sea level rise in most of the oceans, with a 0.1-0.2 mm/yr difference to the trend from the spectral method. Along some of the coastlines of the Northern Hemisphere, the sea level rise computed using ISSM is lower than that using the spectral method by up to 0.2 mm/yr. These trend differences represent less than 8% of the barystatic sea level trend (1.82 mm/yr). For some coastal regions near the melting ice sources (e.g., GrIS, WAIS, Alaska), larger differences (± 0.5 mm/yr) can be found between the two sea level trends, which is about 20% of the barystatic sea level trend.

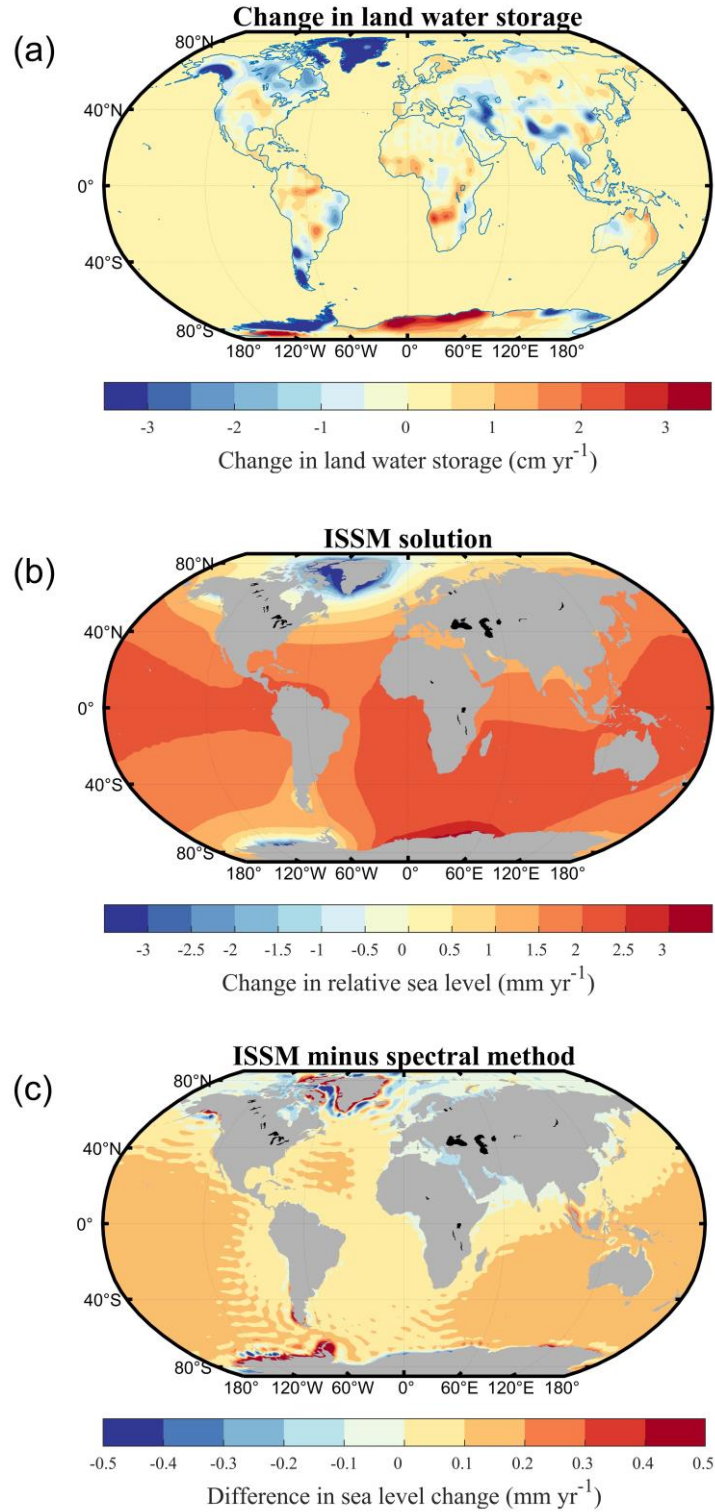


Figure 9. Sea level fingerprints computed by ISSM in response to monthly land water storage change from GRACE data for the period April 2002 to August 2016. **(a)** Linear trends (cm yr^{-1}) in monthly land water storage from GRACE data. **(b)** Linear trends (mm yr^{-1}) in monthly relative sea level change computed by ISSM. **(c)** Difference in sea level linear trends between ISSM and spectral methods (ISSM minus spectral method).

Since the sea level fingerprint driven by GRACE ice mass changes is a consequence of multiple melting sources (e.g., GrIS, AIS), the comparison could not reflect the difference of fingerprints due to one single major ice melting. For this case, we did another comparison of fingerprints which were driven by the simplified melting over each of the GrIS and AIS.

Under the assumption that ice over the GrIS and AIS melts uniformly, we computed the associated relative sea level changes using ISSM. We normalized them by the barystatic sea level change and denoted them as normalized sea level fingerprints. We then compared the normalized sea level fingerprints produced by ISSM with those by the spectral method (Mitrovica et al., 2001) (Fig. 10).

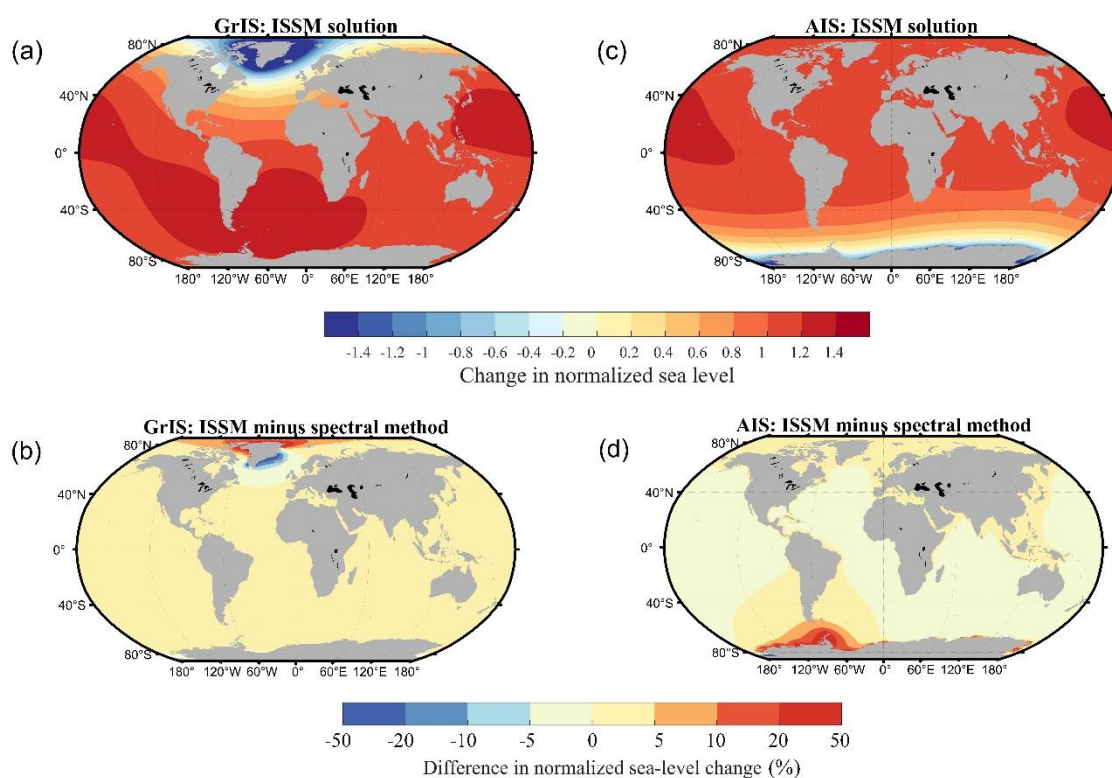


Figure 10. Validation of normalized sea level fingerprints computed by ISSM associated with a uniform thinning of the GrIS (a, b) and AIS (c, d). Panel (a) and (c) show normalized sea level fingerprints computed by ISSM under the GrIS and AIS uniform melting scenarios, respectively. Panel (b) and (d) show difference in normalized sea level fingerprints between ISSM and spectral methods (ISSM minus spectral method).

An obvious sea level fall can be seen in the near fields of the GrIS and AIS, with magnitude larger than 1.4 times the barystatic sea level change (Fig. 10a, c). For both GrIS and AIS melting scenarios, a gradual shift toward positive sea level rise is shown along the distances from the melting ice sheets to the equator. The maximum sea level rise due to uniform thinning of ice sheets is 1.2-1.4 times the barystatic sea level change, in far fields of individual ice sheets. This is a typical pattern in sea level fingerprints primarily resulting from gravity variations and solid earth deformation in response to the ice sheet melting. Besides, there is also a strong rotational effect of ice sheet melting to sea level in far fields, leading to uneven distributions of relative sea level changes (Fig. 10a).

The differences of normalized sea level fingerprints between ISSM and spectral methods (ISSM minus spectral method) are shown in Fig. 10b and 10d. It is evident that a small difference in relative sea level change can be found in most oceans, at a magnitude of less than 10% of the barystatic sea level change. A shift towards larger differences can be found with increasing proximity to the melting ice sheets. The sea level fall in regions close to melt zones shows the difference between ISSM and spectral methods is up to a magnitude of around 50% of the barystatic sea level change. The reasons for the differences in sea level fingerprints computed by ISSM and spectral method in the two comparisons are discussed in section 4.1.

3.2 Resolution test

We next tested the impacts of mesh resolution on the solutions of sea level fingerprints. In this test, we prepared five unstructured meshes which have incremental spatial resolutions (i.e., 100 km, 50 km, 25 km, 10 km, 5 km) for each of the GrIS and AIS domains, respectively. We then computed sea level fingerprints using each of them in turn, forced by high-resolution ice sheet mass changes. Here we chose the high-resolution projections of ice thickness change over the GrIS (2.5 km) and AIS (5 km) in 2100 compared to 2000 under the RCP8.5 scenario (Golledge et al., 2019) (refer to section 2.3.3). For solution comparisons, we normalized the sea level

fingerprints by the barystatic sea level changes and then compared the normalized sea level fingerprints of different resolutions (Fig. 11).

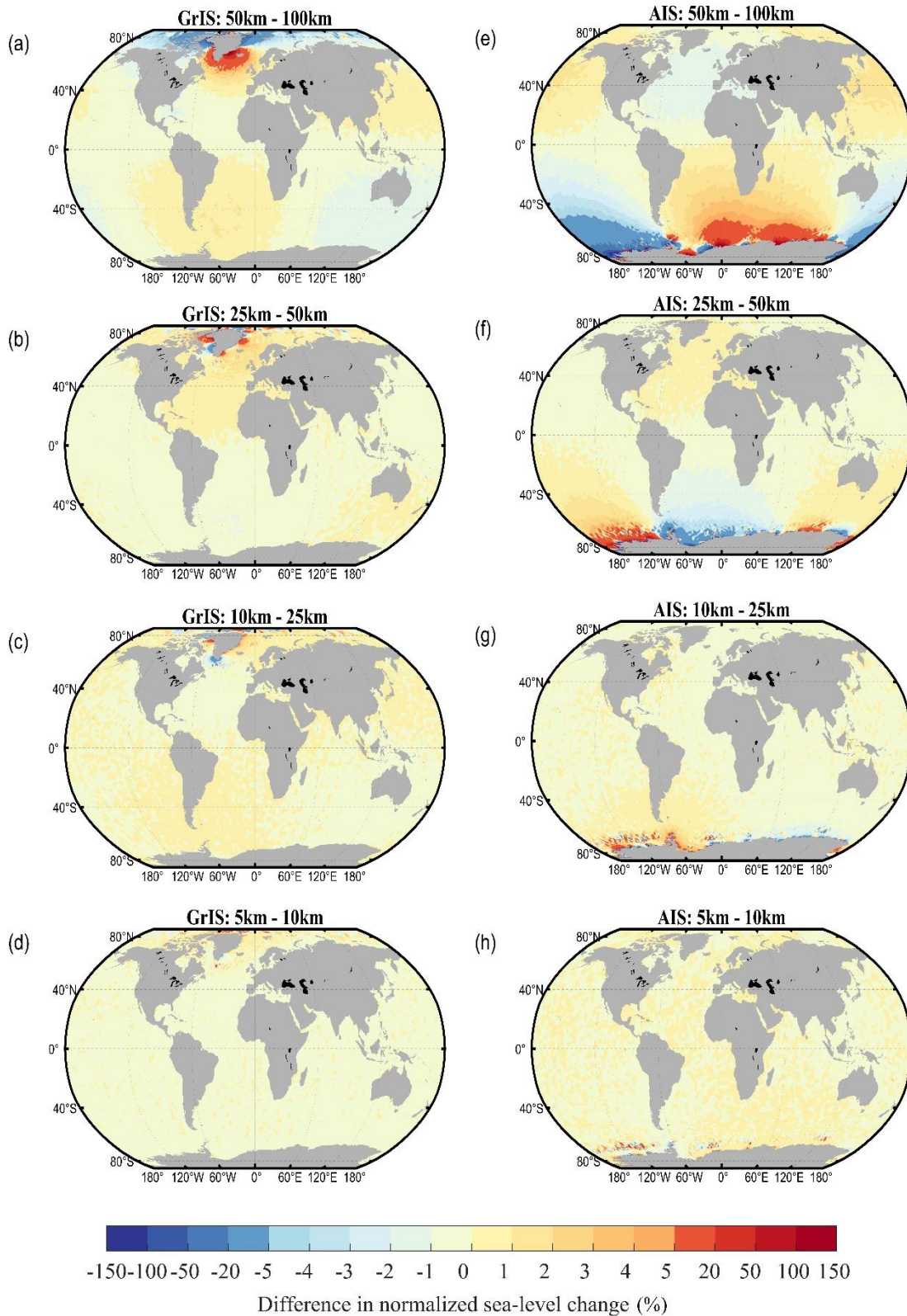


Figure 11. Difference in normalized sea level fingerprints of different resolutions (5 km, 10 km, 25 km, 50 km, 100 km) for the GrIS (a, b, c, d) and AIS (e, f, g, h) domains, in response to high-resolution projected ice thickness change over individual ice sheets (GrIS-2.5 km, AIS-5 km) in 2100 compared to 2000 under the RCP8.5 scenario. Each caption indicates the comparison of fingerprints between two resolutions.

Comparing the solutions between the 50 km and 100 km resolutions (Fig. 11a, e), significant differences are found in sea level fingerprints for coastal regions near to the melting ice sheet, at magnitude of larger than 20% of the barystatic sea level change. Positive differences are evident in areas nearby the southern GrIS and the EAIS, while negative differences are shown in regions near to the northern GrIS and the WAIS. A gradual shift toward smaller difference than 1% of the barystatic sea level change is shown along the distances from the melting ice sheets to the far fields. Additionally, for both ice sheets scenarios, there exists an azimuthal (“semi-hemispheric”) asymmetric pattern in distributions of sea level fingerprint differences. This is associated with the change in the Earth’s rotating axis due to the difference in resolving ice mass changes by 50 km and 100 km resolutions.

The comparison of solutions between the 25 km and 50 km resolutions (Fig. 11b, f) shows that significant differences are limited to regions near to the melt zone. Positive and negative difference can be found in almost all waters surrounding the melting ice sheets. An azimuthal asymmetric pattern is still found in difference of fingerprints.

The comparison of solutions between the 10 km and 25 km resolutions (Fig. 11c, g) shows less significant differences found in coastal regions near to the melt zone, at magnitudes limited to 20% of the barystatic sea level change. Additionally, the azimuthal asymmetric difference distributions become more subtle than the previous comparisons.

The comparison between solutions using the 5 km and 10 km resolutions (Fig. 11d, h), shows almost all differences globally are limited to 5% of the barystatic sea level change. There are also no obvious differences in the semi-hemispheric signal due to differences in the Earth’s rotating axis between the solutions. Given uncertainties in mass loading datasets, the differences between solutions with 10 km and 5 km resolution are negligible.

We also compared the computational effort for the different resolutions, considering the numbers of vertices, elements and calculation time of each ISSM mesh used for sea level

computation (Table. 1). With increased resolution, the numbers of vertices and elements in ISSM meshes and computation time increases. A dramatic rise in these three variables can be found from the 10 km to 5 km resolutions, with the AIS computations at 5 km taking approximately 10 days on a high-end Linux desktop. By contrast, the solution using 10 km resolution took less than 1 day. Considering the similarity of solutions between the 5 km and 10 km resolutions and high computation requirement for the 5km grid, we chose to use the ISSM mesh with 10 km resolution over the polar ice sheets for our future sea level fingerprint computations.

Table 1. Computation resources of ten ISSM meshes used in resolution test, including numbers of vertices, elements of ISSM mesh and computation time.

ISSM Meshes	Number of vertices	Number of elements	Computation time (h)
A. Five ISSM meshes with incremental resolutions over the GrIS			
A1. GrIS-100 km	19535	39066	0.1
A2. GrIS-50 km	21036	42068	0.2
A3. GrIS-25 km	27247	54490	0.2
A4. GrIS-10 km	68879	137754	1.5
A5. GrIS-5 km	228986	457968	16.2
B. Five ISSM meshes with incremental resolutions over the AIS			
B1. AIS-100 km	20689	41374	0.1
B2. AIS-50 km	26570	53136	0.2
B3. AIS-25 km	52512	105020	0.9
B4. AIS-10 km	227037	454070	15.5
B5. AIS-5 km	910172	1820340	245.1

3.3 Sensitivity test to 1-D elastic Earth models

To investigate the sensitivity of sea level fingerprints to different 1-D elastic Earth models, we computed sea level fingerprints in response to uniform thinning of the GrIS and AIS with three 1-D elastic Earth models: PREM, ak135 and iasp91 respectively (refer to section 2.3.2). For comparison, we scaled the sea level fingerprints by the barystatic sea level change (i.e., normalized sea level fingerprints) and then made differences between PREM and the other two Earth models (Fig. 12). Fig. 12a and 12d show the normalized sea level fingerprints computed using the PREM Earth model in response to uniform thinning of the GrIS and AIS, respectively.

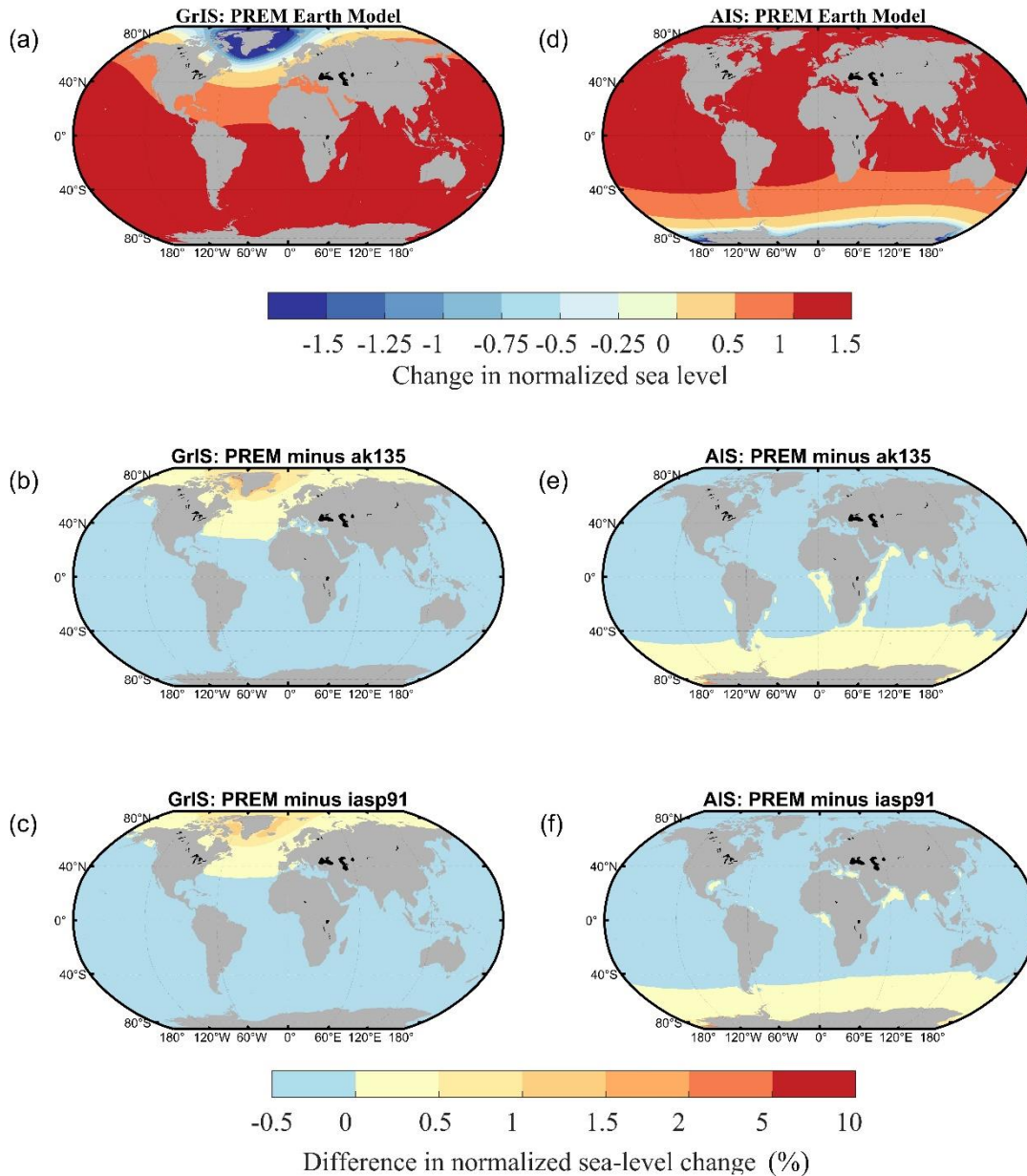


Figure 12. Comparisons of normalized sea level fingerprints computed with PREM, iak135 and iasp91 1-D elastic Earth models, in response to uniform thinning of the GrIS (a, b, c) and AIS (d, e, f). Panel (a) and (d) show normalized sea level changes computed on PREM Earth model. Panel (b) and (e) show difference in normalized sea level fingerprints between PREM and ak135 Earth models for the GrIS and AIS melting scenarios, respectively. Panel (c) and (f) show difference in normalized sea level fingerprints between PREM and iasp91 Earth models for the GrIS and AIS melting scenarios, respectively.

The differences of sea level fingerprints due to different 1-D elastic earth models, in response to the identical uniform thinning of the GrIS are shown in Fig. 12b (PREM minus ak135) and

12c (PREM minus iasp91). Overall, the sea level fingerprints computed using different 1-D elastic Earth models are almost the same, with differences smaller than 5% of the barystatic sea level change. The differences of fingerprints have an evident shift towards smaller values in the far fields of melting ice sheets compared to the near fields. Specifically, the difference on sea level fall in the near field of the GrIS drops quickly from a magnitude of +5% to +0.5% of the barystatic sea level change. In the far field of the GrIS, where sea level gradually rises, the difference decreases smoothly from +0.5% to -0.5% of the barystatic sea level change. This is associated with a decrease in difference of Earth's surface deformations between the Earth models along the distances from the melting ice sheets.

Similarly, the variation of sea level fingerprints due to different 1-D elastic Earth models, in response to the identical uniform thinning of the AIS is shown in Fig. 12e (PREM minus ak135) and 12f (PREM minus iasp91). Again, the variation is small with a maximum of 5% of the barystatic sea level change in sea level fingerprints. There is a smooth decrease in the difference of sea level change from near fields to far fields of the AIS, with a magnitude from +0.5% to -0.5% of the barystatic sea level change. Larger differences are only found in small coastal regions near the melt zones, with a magnitude of 5% of the barystatic sea level change.

3.4 Future sea level fingerprints associated with polar ice sheets melting

Based on findings from our resolution tests, we adopted PREM 1-D elastic Earth model and the optimal ISSM mesh (i.e., 10 km resolution for the GrIS and AIS domains) to compute high-resolution sea level fingerprints in response to every 5-year ice thickness change over individual polar ice sheets in the 21st century under the RCP4.5 and RCP8.5 scenarios. The linear trends of sea level fingerprints in the 21st century are presented in Fig. 13.

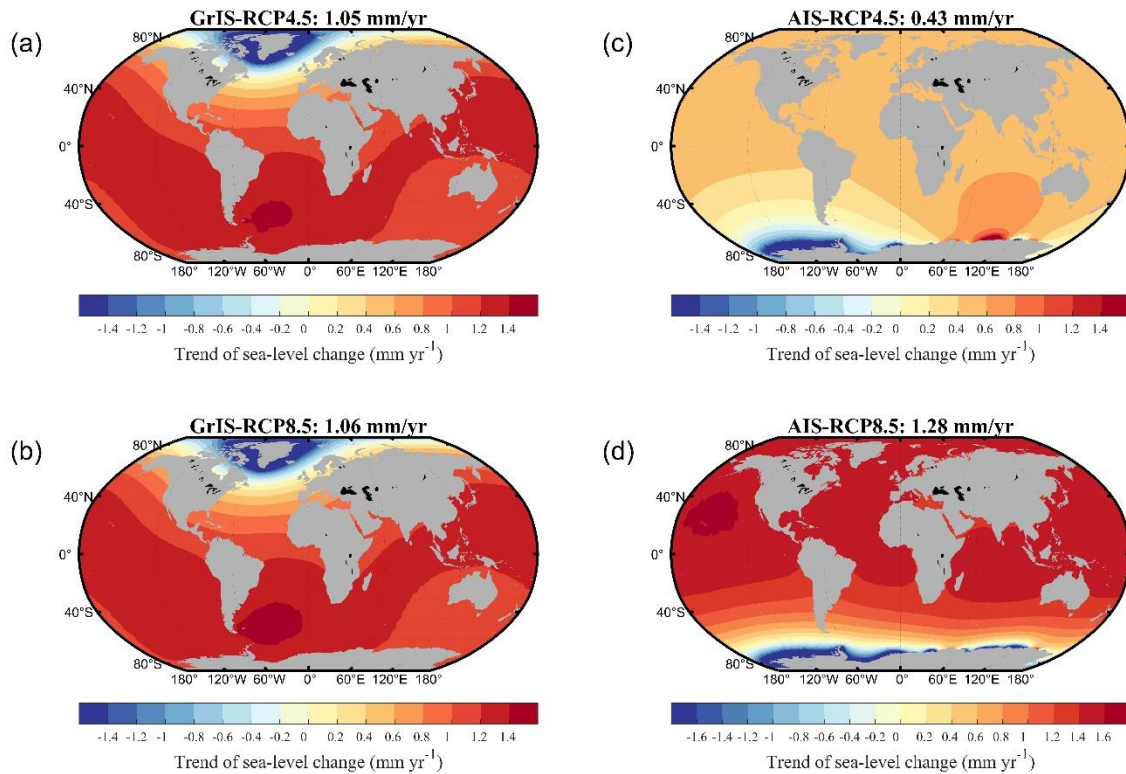


Figure 13. Linear trends in future sea level fingerprints (mm yr^{-1}) associated with individual polar ice sheets melting during the period 2000-2100 under the RCP4.5 (**a**-GrIS, **c**-AIS) and 8.5 (**b**-GrIS, **d**-AIS) scenarios. The barystatic sea level trend (mm yr^{-1}) under each melting scenario in the 21st century is shown on top of each panel.

In the case of GrIS melting under the two RCP scenarios (Fig. 13a, b), there are very similar projections of the barystatic sea level trend, and regional pattern of sea level fingerprints which is characterized by a sea level fall in the near field of the ice sheets and a gradually increasing sea level rise in far fields at greater distances from the ice sheets. The maximum sea level trend is projected in the Southwest Atlantic Ocean where local sea level will experience over 1.4 mm rise per year over the period 2000-2100. Note that this is only due to ice sheet melting and no small glaciers, hydrology or thermal expansion.

In the case of AIS melting, sea level changes differ substantially between the two RCP scenarios, in terms of both the barystatic sea level trend and spatial variations (Fig. 13c, d). The

projected barystatic sea level trend under the RCP8.5 scenario in the 21st century is 1.25 mm/yr, which is almost three times the value under the RCP 4.5 scenario.

Under RCP4.5 (Fig. 13c), there is a significant sea level fall and rise in the near field of the WAIS and EAIS margins, respectively. A gradual shift from a sea level fall to a sea level rise can be seen with increasing distances from the WAIS, while with increasing distances from the EAIS the sea level rise is smoothly decreasing. In the far field of the AIS, the sea level rise reaches ~0.5 mm/yr.

The spatial pattern in sea level fingerprints under RCP8.5 is characterized by a substantial sea level fall in the near field of the whole AIS and a gradual shift to positive sea level rise in the far field (Fig. 13d). The maximum sea level rise in the far field is found in the North Pacific Ocean, at magnitude of around 1.6 mm/yr which is 1.25 times the barystatic value.

3.5 Kernel-based sea level projections

Local sea level change induced by melting of polar ice sheets can be derived by summing up sea level contributions from the individual ice sheet drainage basins. Here we used kernel-based sea level projection to provide sea level contributions in the 21st century from each basin over GrIS and AIS for ten selected coastal cities globally (Fig. 14, 16) under the RCP4.5 and RCP8.5 scenarios. In kernel-based sea level projections, we combined future ice thickness changes and site-specific sea level sensitivity kernels to derive local sea level contributions from each drainage basin. The quantifications of these variables in individual basins over the GrIS and AIS are shown in Fig. 15 and Fig. 17, respectively.

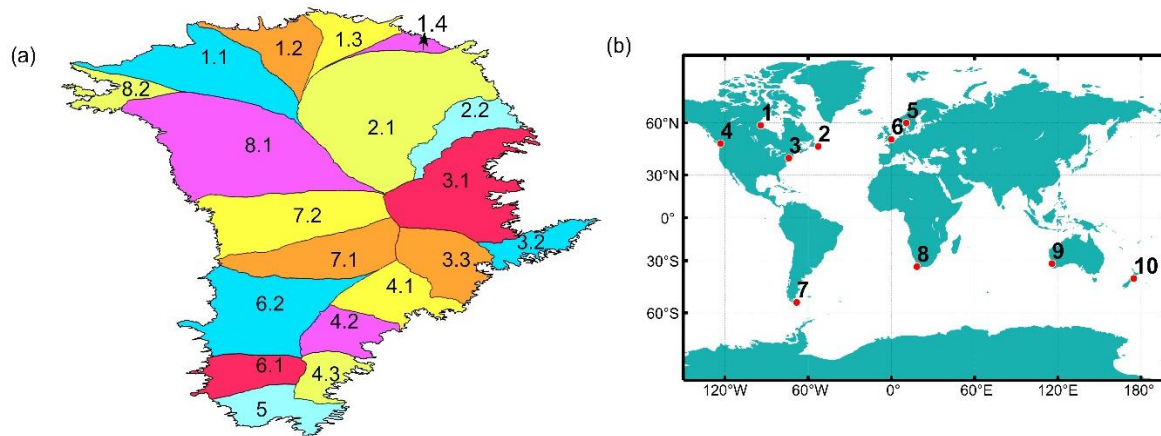


Figure 14. Maps of the GrIS drainage basins (a) and the selected cities (b). The numbers in the basin map (a) are referred to as basin ID numbers (Zwally et al., 2012). The numbers in the city map (b) are referred to the selected cities in Fig. 15 (1- Churchill, Canada, 2- St. Johns, Canada, 3- New York, U.S., 4- Vancouver, Canada, 5- Oslo, Norway, 6- London, U.K., 7- Ushualia, Argentina, 8- Cape Town, South Africa, 9- Perth, Australia, 10- Wellington, New Zealand).

There is a similar spatial pattern in ice thickness change over the GrIS in the 21st century under RCP4.5 and RCP8.5 (Fig. 5, 15a). Substantial loss of ice can be found in northwestern (basins 1.1, 8.1, 8.2) and southeastern GrIS (basins 4.2, 4.3), with area-averaged ice thickness reductions of more than 40 m in each basin. Moderate ablation of ice takes place in the southwestern (basins 5, 6.1, 6.2, 7.1) and the northeastern GrIS (basins 2.1, 2.2, 3.1, 3.2, 3.3), with a ~10 m ice thickness reduction in each basin. Compared to RCP4.5, there is a contrast between north and south in terms of ice thickness reduction over the GrIS in the higher emission forcing (RCP8.5), with more ice loss in the northern GrIS (basins 8.1, 8.2, 1.1, 1.2, 1.3, 1.4) and less ice loss in southern GrIS (basins 4.2, 5, 6.1, 6.2, 7.1).

To quantify the sensitivity of sea level at different coastal cities to melting in each basin, we used site-specific kernel sensitivity to project local sea level rise at selected coastal cities under the assumption that ice thickness over the GrIS basins reduced by 1 meter uniformly (Fig. 15b). Sea level sensitivities of four selected cities in the Southern Hemisphere (i.e., Ushuaia, Perth, Cape Town and Wellington) are similar to each other. This is because their locations are all distant from the GrIS so that there is little distinction between their sea level sensitivities to the

melting over GrIS basins. For these cities, the sensitivities are all positive for each basin, with maximum (0.8 mm local sea level rise per 1m of uniform ice thickness thinning in basin) and minimum (0 mm/m) value in basin 2.1 and 1.4, respectively. While for six selected cities in the Northern Hemisphere (i.e., Churchill, St. Johns, New York, Vancouver, Oslo, London), they have distinct sensitivities for each basin. Sensitivities of New York and Vancouver are positive to melting in all basins, with maximum value (0.4 mm/m) in basin 2.1. For London and Churchill, there are small positive sensitivities found for most GrIS basins, with a value below 0.2 mm/m, except for a slightly negative sensitivity (0.05 mm local sea level fall per 1 m of uniform ice thickness thinning in basin) of Churchill to basin 8.1. For Oslo and St. Johns, apart from showing little sensitivity to most GrIS basins, there are small negative sensitivities found in the northeastern GrIS basins 2.1, 3.1 and the southern GrIS basins 4.2, 4.3, 5, 6.1, 6.2, respectively, all at magnitude of 0.1 mm/m.

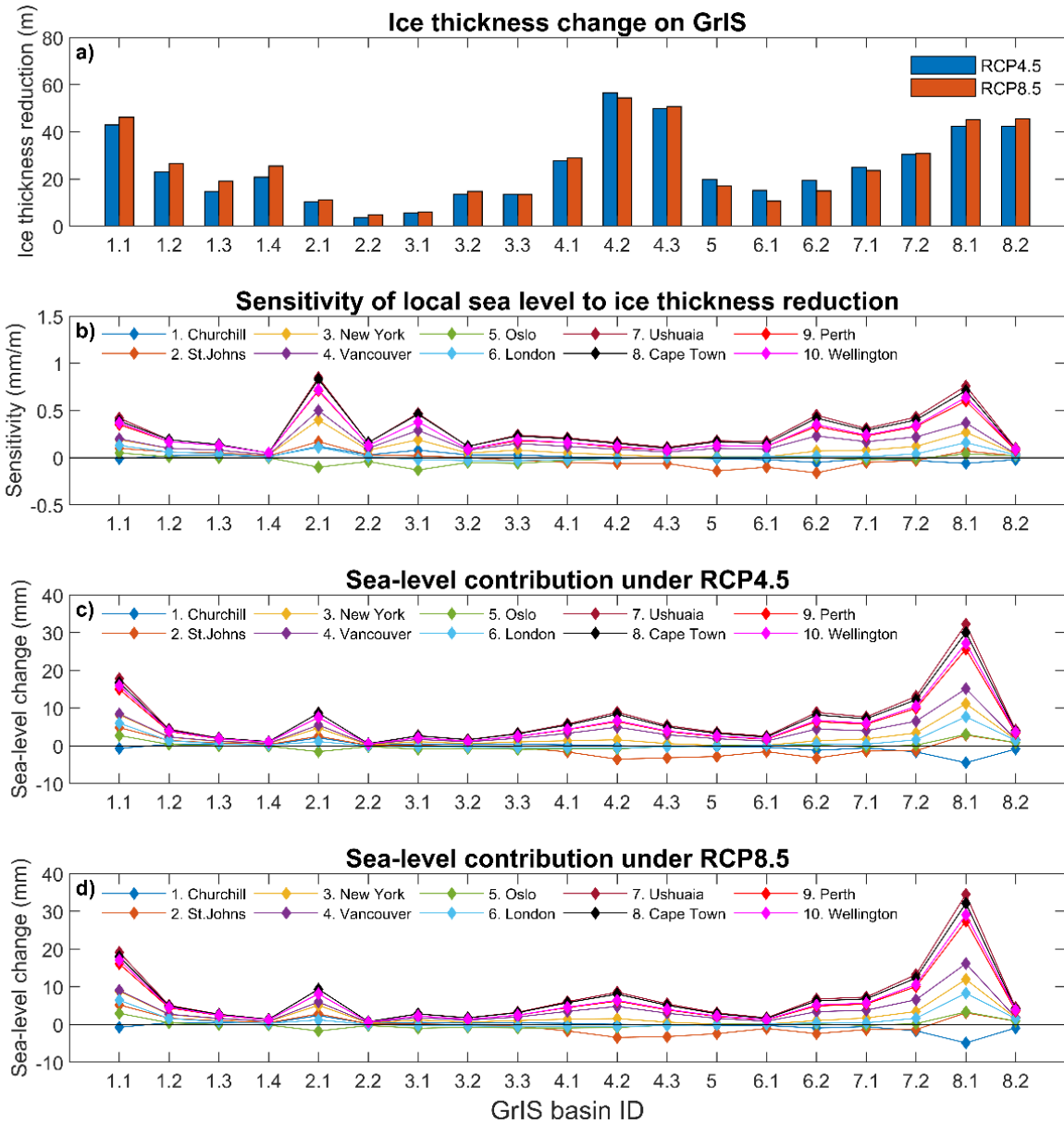


Figure 15. Future kernel-based projection of sea level in the 21st century for each of 19 drainage basins of the GrIS (see Fig. 14a for GrIS drainage basin definition). Panel (a) presents the area-averaged ice thickness changed in 2100 compared to 2000 under the RCP4.5 and RCP8.5 scenarios. Panel (b) presents the local sea level changed for selected coastal cities due to uniform one-meter ice thickness reduction over each GrIS basin (see Fig. 14b for coastal city locations). Panels (c) and (d) present kernel-projected contributions to local sea level for the selected coastal cities in the 21st century under RCP4.5 and RCP8.5, respectively.

The kernel-based sea level projections for selected cities from GrIS drainage basins in the 21st century under the RCP4.5 and 8.5 scenarios are shown in Fig. 15c and 15d, respectively. We found the sea level contributions to each selected city by GrIS basins are affected by two factors: ice thickness change in basins and a city-specific sea level sensitivity.

Due to the similar positive sensitivity to melting in GrIS basins, the cities in the Southern Hemisphere experience similar positive sea level contributions (i.e., local sea level rise) from GrIS basins. Since there is distinction in future projections of ice thickness change in GrIS basins in the 21st century, so the projected sea level contributions to the cities differ by each GrIS basin. Specifically, the most sea level contributions are found in basin 8.1 (30 mm) and basin 1.1 (18 mm), in the northwestern GrIS where substantial ice thickness reduction is projected. Other individual basins give less positive sea level contributions, ranging from 12 mm (basin 7.2) to 0 mm (basin 1.4), due to either smaller sea level sensitivity or less ice thickness reduction. For example, there is significant ice thickness reduction in basin 4.2 in the southeastern GrIS, but it has the same sea level contributions as basin 2.1 in the northeastern GrIS where small ice loss occurs. It is because the cities in the Southern Hemisphere have smaller sea level sensitivities to the melting in basin 8.1 compared to basin 2.1.

The cities in the Northern Hemisphere have distinct sea level sensitivities for each GrIS basin. Besides, the future projections of ice thickness change in the GrIS basins in the 21st century are also different. Therefore, two factors (i.e., projected ice thickness change in a drainage basin and sensitivity of one city's sea level to this basin's ice change) make the projected sea level contributions to the selected cities in the Northern Hemisphere distinct from both of cities and the GrIS basins. Specifically, sea levels of New York and Vancouver are more sensitive to northern GrIS basins 8.1, 2.1 and 3.1 than other basins, but only basin 8.1 of the three basins experiences large ice loss. Therefore basin 8.1 contributes the most (15 mm) to the cities and other individual basins give smaller positive contributions (<10 mm). Since little sensitivities are found at London to all GrIS basins, therefore London experiences small sea level contributions from each GrIS basin, with maximum contributions up to 8 mm from the

northwestern GrIS basins 8.1 and 1.1. Similarly, there is little contribution found from most GrIS basins at St. Johns, Churchill and Oslo due to little sensitivities. But small negative contributions (i.e., local sea level fall) to sea level are found in the southern GrIS (basins 4.2, 4.3, 5) for St. Johns (-3 mm) and the northwestern GrIS (basin 8.1) for Churchill (-5 mm) and the northeastern GrIS (basin 2.1) for Oslo (-1 mm). This is because these cities have small negative sea level sensitivities to the melting in those basins (Fig. 15b).

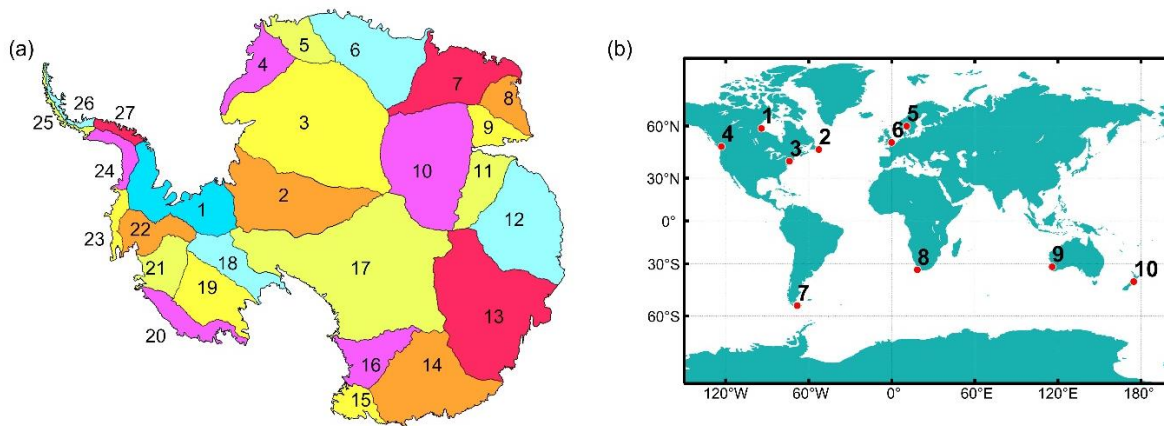


Figure 16. Maps of the AIS drainage basins (a) and the selected cities (b). The numbers in the basin map (a) are referred to as basin ID numbers (Zwally et al., 2012). The numbers in the city map (b) are referred to the selected cities in Fig. 17 (1- Churchill, Canada, 2- St. Johns, Canada, 3- New York, U.S., 4- Vancouver, Canada, 5- Oslo, Norway, 6-London, U.K., 7-Ushualia, Argentina, 8-Cape Town, South Africa, 9-Perth, Australia, 10- Wellington, New Zealand).

For Antarctic melting, an evident difference in ice thickness change can be found over each AIS basin under the RCP4.5 and RCP8.5 scenarios (Fig. 5, 17a). Under RCP4.5, substantial loss of ice occurs along the coasts of the WAIS (basins 20-25). Small ice gain is found in the EAIS margins (basins 12, 15-16) and the Antarctic Peninsula (basins 26, 27). Over the rest of the basins in Antarctica, very little ice thickness change occurs in the projection by 2100. Compared to RCP4.5, there is more loss of ice over the AIS under RCP8.5. An increase in ice loss is found along the WAIS margins (basins 20-24, 26), especially in basin 20 where rapid reduction in ice thickness is seen (over 10 m). A widespread melting occurs at the EAIS margins

(basins 4-9, 12-13), especially in basin 4 where rapid ice thickness reduction is projected (over 12 m).

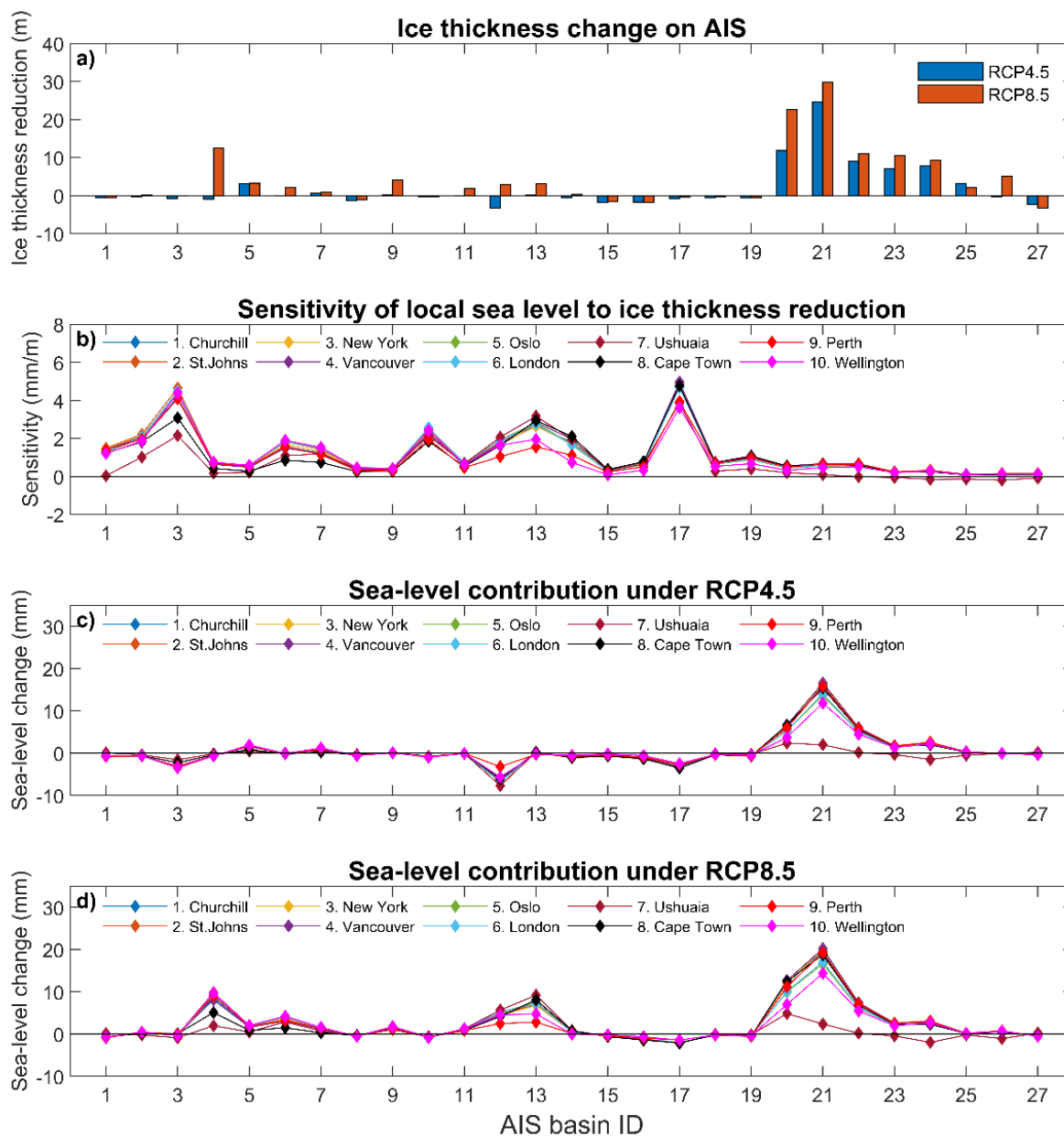


Figure 17. Future kernel-based projection of sea level in the 21st century for 27 drainage basins of the AIS (see Fig. 16a for AIS drainage basin definition). Panel (a) presents the area-averaged ice thickness changed in 2100 compared to 2000 under the RCP4.5 and RCP8.5 scenarios. Panel (b) presents the local sea level changed for the selected coastal cities due to a uniform one-meter ice reduction over each of the AIS basins (see Fig. 16b for coastal city locations). Panels (c) and (d) present kernel-projected contributions to local sea level for the selected coastal cities in the 21st century, under RCP4.5 and 8.5, respectively.

The sea level change associated with uniform melting in each AIS basin (i.e., ice thickness uniformly reduced by 1m) at selected cities reflects the sensitivity of local sea level rise at cities to ice melting in individual basins (Fig. 17b). Being located in the far field of the AIS, the selected cities in the Northern Hemisphere (i.e., Churchill, St. Johns, New York, Vancouver, Oslo, London) have similar sensitivities for each basin, with maximum and minimum values in basin 17 in the southern AIS (5 mm/m) and basins 23-27 in the Antarctic Peninsula (0 mm/m), respectively. For the selected cities in the Southern Hemisphere, their sensitivities differ in each basin. Local sea level at Ushuaia and Cape Town is most sensitive to basin 17 in the southern AIS (5 mm/m), while for Perth and Wellington the maximum sensitivities are found in basin 3 in the northern AIS (5 mm/m).

The kernel-projected sea level contributions for the selected cities from AIS basins in the 21st century under the RCP4.5 and 8.5 scenarios are shown in Fig. 17c and 17d, respectively. Similarly, we found the sea level contributions to each selected city by AIS drainage basins are affected by the two factors: projected ice thickness change in a drainage basin and sensitivity of one city's sea level to this basin's ice change.

Due to the substantial ice loss in the coast of WAIS (basins 20-24), the most significant sea level contribution for almost all selected cities is from these basins, which accounts for around 30 mm of sea level rise by 2100. The exception is Ushuaia (3 mm) because of its small sea level sensitivity. Under RCP4.5, there is a general negative contribution to local sea level change at all selected cities from basins 12 in the EAIS, ranging from -2 mm for Perth to -9 mm for Ushuaia. It is caused by the combination of positive sea level sensitivity to ice thickness reduction (i.e., negative sea level sensitivity to ice thickness increase) and ice mass gain in this basin. Compared to RCP4.5, there is intensified ice loss along the coasts of AIS basins under RCP8.5, which leads to larger sea level contributions to almost all of the selected cities. An evident increase of total sea level contributions is found in the northern AIS basins 3-6 for all selected cities, from 0 mm under RCP4.5 to around 15 mm under RCP8.5. Along the EAIS margins basins 12-14 change from a negative (-5 mm) to a positive (15 mm) total sea level

contribution in the higher emission forcing for all selected cities. The sea level contribution from WAIS (basins 20-24) to all selected cities is also intensified under RCP8.5, which accounts for around 40mm sea level rise, except for small sea level contributions to Ushuaia (5 mm).

4. Discussions

4.1 Validation on ISSM-SESAW computation

By comparing sea level fingerprints computed using ISSM-SESAW and previously published results using the spectral method (Mitrovica et al., 2001, Adhikari et al., 2019), we validated the solutions in ISSM-SESAW computation.

Here, we did two comparisons using different input datasets. Firstly, we compared the linear trends of sea level fingerprints driven by monthly land water storage change from GRACE data for the period April 2002 to August 2016. In this comparison, small differences ($< 8\%$ of the barystatic sea level trend) in fingerprints were found for most areas. But a large difference ($\sim 20\%$ of the barystatic sea level trend) existed in the fingerprints along the coastlines of major sources of ice melt (e.g., GrIS, WAIS, Alaska glaciers, Patagonia glaciers). It is likely associated with the remapping from GRACE ice mass change input to ISSM mesh grids. Compared to the spectral methods, ISSM-SESAW needs to remapped GRACE ice mass changes data from uniformly distributed pixel grids to unstructured mesh grids as input of ISSM models. The remapping produces the errors in sampling of ice mass changes, which subsequently causes some differences in sea level fingerprints in the near fields of the major melting sources.

We also compared the sea level fingerprints in response to uniform melting of each of the GrIS and AIS between ISSM-SESAW and the spectral method. Fingerprints are almost the same for most areas, except for larger differences ($\sim 50\%$ of the barystatic sea level change) in the near fields of melting ice sheets. This is because the ISSM mesh resolves coastlines of melting ice sheets differently compared to the spectral method. The ISSM mesh has advantages in resolving more accurate coastlines than spectral methods due to its unstructured mesh-grid design. Based on a function of distance from the nearest coastlines, the ISSM mesh could be flexibly refined near the coastlines. Therefore, ISSM mesh could capture more ice melting input at regions near coastlines and improve the accuracy of sea level fingerprints in ISSM-SESAW computations.

Overall, in two comparisons, all differences in sea level fingerprints between ISSM-SESAW and the spectral method are less than 10% of barystatic sea level change for most areas and are limited to 50% of barystatic sea level change in regions close to melting sources (within ~300 km). The relatively large difference in near fields of the melting sources is due to the distinction of grids employed in the two methods. Therefore, we demonstrated that the sea level fingerprints computed by ISSM-SESAW are similar to those computed by the spectral method. Therefore, the solutions in ISSM-SESAW computations are validated.

4.2 Resolution test

By using flexible unstructured mesh grids, we did a further experiment to explore the sensitivity of sea level fingerprints computed using the ISSM-SESAW module to representation of melting ice sheets with different resolutions. We prepared five ISSM meshes with incremental resolutions (100 km, 50 km, 25 km, 10 km and 5 km) for each of the GrIS and AIS domains and adopted them individually compute sea level fingerprints in response to high-resolution polar ice sheet melting in the 21st century.

By comparing the outputs using pairs of resolutions, we found a gradual convergence in computed sea level fingerprints with increasing resolutions. In the far fields of melting ice sheets, there is a semi-hemispheric asymmetric pattern in differences of fingerprint associated with rotation feedback (Milne & Mitrovica 1998). It arises from the increase of accuracy in sampling of melt geometry in polar ice sheets due to incremental resolutions. However, the effect on amplitude of far-field sea level fingerprints due to various polar ice sheet resolutions is always small (<5% of the barystatic sea level change). In the near fields of melting ice sheets, there is a significant difference of fingerprints between the 10 km and 100 km resolutions (>50% of the barystatic sea level change). This is likely because compared to the 100 km resolution, more mass changes are captured in the 10 km resolution and they have strong impacts on near-field sea level changes by large perturbations in the local solid Earth deformations and local

gravity fields (Farrell and Clark, 1976). We also did a comparison between the 5 km and 10 km resolutions, but there is trivial (~5% of the barystatic sea level change) difference in fingerprints for most regions.

We also considered the computational time for different resolutions. For the 5 km resolution the computation time are 16.2 and 245.1 hours for GrIS and AIS melting scenarios, respectively, which are both 16 times larger than the time for the 10 km resolution. Therefore, we concluded that the 10km resolution is the optimal resolution for each polar ice sheet to capture details of future mass changes and also save large computational time.

4.3 Sensitivity test to 1-D elastic Earth models

We tested the sensitivity of sea level fingerprints to different crustal structures in 1-D elastic Earth models. We adopted three different 1-D elastic Earth models PREM, iasp91 and ak135 to compute sea level fingerprints in response to uniform melting of each polar ice sheet. The main differences of the three Earth models are the discontinuity in elastic structures at depths of 220 km in PREM and gaps of physical parameters in the crust and the top of the mantle between PREM and the other two Earth models (Wang et al., 2012).

By comparing PREM with either iasp91 or ak135 Earth model, we found there exists differences in sea level fingerprints due to the choice of 1-D elastic Earth models, especially for the difference in coastal regions of the melting ice sheets (~5% of the barystatic sea level change). It is mostly associated with distinction in near-field response of the Earth's crustal structures to the loading scenarios given in various 1-D elastic Earth models. Wang et al. (2012) indicated that there are significant differences between PREM and both of iasp91 and ak135 Earth models in Earth surface deformations (e.g., ~26% for radial displacement, ~25% for gravity change), especially for near-field regions ($\theta < 1^\circ$) in response to loading variations. However, in comparison between ak135 and iasp91 Earth models, the computed sea level fingerprints are very similar to each other. This is presumably due to there being no significant

differences of Earth surface deformations (e.g., ~3% for radial displacement, ~2% for gravity change) between the two Earth models (Wang et al., 2012). Overall, all differences in sea level fingerprints due to different 1-D elastic earth models are negligible for most regions. Therefore, we concluded that sea level fingerprints are insensitive to different crustal structures in 1-D elastic Earth models.

4.4. Future sea level fingerprints in response to projected polar ice sheet mass changes

Based on the findings in previous sensitivity tests, we adopted the ISSM mesh with 10 km resolution in polar ice sheets and used PREM 1-D elastic Earth model to compute future sea level fingerprints driven by each polar ice sheet melting in the 21st century under the RCP4.5 and 8.5 scenarios.

We found that the barystatic sea level trend and regional sea level distributions due to GrIS melting over the period 2000-2100 are very similar under the two RCP scenarios. This is a consequence of the similar pattern in projected mass changes over the GrIS in this century under RCP4.5 and 8.5. In the 21st century, a widespread mass loss is projected over the GrIS, with a substantial ice thickness reduction along the southeast and northwest margins as well as a thinning in the northeast portions (Golledge et al., 2019). Consequently, there is substantial sea level fall in the near field and a gradual sea level rise towards the far field, which is similar to the regional sea level distributions in response to the GrIS uniform melting. However, for AIS melting over the period 2000-2100, the resulting barystatic sea level trend and regional distributions show strong differences under the two RCP scenarios. Firstly, the barystatic sea level trend due to AIS melting under RCP8.5 is three times larger than that under RCP4.5. It is associated with widespread thinning and increased calving over the AIS in response to higher greenhouse gas emissions under RCP 8.5 compared to RCP4.5 (Golledge et al., 2019). Secondly, due to different mass change projections, AIS melting in the 21st century under the two RCP scenarios leads to distinct patterns in regional sea level changes. One evident example

is the opposite sea level change pattern in the near field of the EAIS projected under the two RCP scenarios. Under RCP4.5, driven by moderate mass gain over Queen Mary Land in the 21st century, there is a significant sea level rise predicted in the near field of the EAIS. But under RCP8.5, forced by high greenhouse emissions, intensified basal and dynamic mass loss is projected to occur on the coastlines of Queen Mary Land in the 21st century (Golledge et al., 2019). Therefore, under the RCP8.5 scenario a sea level fall is expected in the near field with a gradual shift to sea level rise in the far field of the EAIS. Besides, a substantial sea level fall is predicted in the near field of the WAIS in this century under both RCP scenarios. This is due to the greatest thickness changes over the AIS occurring in the grounded ice of the Amundsen Sea sector of West Antarctica in this century (Golledge et al., 2019).

In our study, the estimates of the barystatic sea level change due to GrIS and AIS melting in 2100 compared to 2000 for RCP 4.5 are 0.11 m and 0.04 m, respectively, and for RCP8.5 are 0.11 m and 0.13 m, respectively. We found good consistency of our barystatic sea level change solutions with the global mean sea level contributions given in previous studies.

Church et al. (2013) indicated that the 5% to 95% ranges of future contributions of GrIS and AIS to global mean sea level rise in 2081-2100 relative to 1986-2005 for RCP4.5 are 0.04 to 0.13 m and -0.04 to 0.13 m, respectively, and for RCP8.5 are 0.07 to 0.21 m and -0.06 to 0.12 m, respectively. By comparing to the contributions provided by Church et al. (2013), only slightly larger sea level contributions from the AIS melting in the 21st century for RCP8.5 are found in our study. These differences mainly result from the meltwater feedback included in our data of future projections of the AIS in the 21st century. By trapping the warm water below the sea surfaces, meltwater from Antarctica causes a positive feedback to the Antarctic ice loss, which intensifies the Antarctic dynamical thinning under RCP8.5 (Golledge et al., 2019). Therefore, it leads to larger global mean sea level contributions than the contributions by Church et al. (2013) in which meltwater feedback is not considered (Golledge et al., 2019).

There are other studies which provided global mean sea level contributions of polar ice sheets in the 21st century, accounting for the likelihood of high-risk, low-probability conditions (e.g., rapid ice mass loss of the AIS) (Kopp et al., 2014, Grinsted et al., 2015, Jevrejeva et al., 2019). By means of probability density functions, Kopp et al. (2014) provided the likely ranges (17% to 83% percentile) of the future contributions of GrIS and AIS to global mean sea level rise in the 21st century, which are 0.04 to 0.15m and -0.05 to 0.16m for RCP4.5, respectively, and 0.08 to 0.25m and -0.08 to 0.15m for RCP8.5, respectively. By comparing the results provided by Kopp et al. (2014), we found our solutions of global mean sea level contributions by the GrIS and AIS during the period 2000-2100 are all included in their likely ranges (17% to 83% percentile).

4.5 Kernel-based sea level projections

By means of kernel projections, in this study we calculated local sea level contributions at 10 selected coastal cities from individual drainage basins of the polar ice sheets during the 21st century. We found the sea level contributions to each coastal city from basins are not consistent to either ice thickness change in basins or a city's sea level sensitivities to basins. Instead, sea level contributions to each coastal city is influenced by a combination of both factors. One example of this is the comparison between sea level contributions to Perth from basin 4.2 and basin 8.1 in the southeastern and northwestern GrIS, respectively. There is more ice loss predicted in basin 4.2 (54.39 m area-averaged ice thickness reduction) compared to basin 8.1 (45.23 m area-averaged ice thickness reduction) in the 21st century under RCP8.5 scenario, but basin 8.1 is projected to have a larger sea level contribution to Perth than basin 4.2 (6.22 mm for basin 4.2, 27.39 mm for basin 8.1). This is mainly due to smaller sea level sensitivity of Perth to melting in basin 4.2 than basin 8.1 (0.11 mm/m for basin 4.2, 0.60 mm/m for basin 8.1). In kernel-based projection, multiplying quite small sea level sensitivities and large ice thickness variations eventually derives small sea level contributions. This explains the smaller contributions from basin 4.2 in comparison to basin 8.2 to sea level rise at Perth.

Another significant factor for sea level contributions is ice thickness change in a single basin as it varies between scenarios. One good example is that basin 12 in the EAIS results in an opposite sign of sea level contributions at Perth when comparing RCP4.5 and RCP 8.5 scenarios (3.19 mm local sea level fall under RCP4.5, 2.51 mm local sea level rise under RCP8.5). The sea level sensitivity of Perth to basin 12 is constant (1.05 mm/m). But there are opposite ice thickness changes in basin 12 predicted between two RCP scenarios (3.34 m area-averaged ice thickness increase under RCP4.5, 2.94 m area-averaged ice thickness reduction under RCP8.5), which leads to opposite sea level contributions to Perth. Therefore, we conclude that both sea level sensitivity and ice thickness changes are crucial for projections of local sea level contributions.

Due to the sea level sensitivity factor, coastal cities should pay more attention to ice melting at further distances. For examples, the cities close to the GrIS (e.g., St. Johns, Churchill, Oslo) should not worry about the melting in their nearby basins. It is because the melting in the nearby basins would not contribute to the future sea level rising at neighbouring cities due to negative sea level sensitivity. Compared to the cities in the Northern Hemisphere, coastal cities in the Southern Hemisphere (e.g., Perth) have all positive and larger sea level sensitivity to the GrIS melting and therefore they will experience larger sea level contributions from melting in the GrIS basins in the 21st century. Similarly, coastal cities in the Northern Hemisphere (e.g., London) will experience larger sea level contributions from melting in the AIS basins in the 21st century.

Additionally, if thickness change factor is included, each coastal city should monitor basins where there is both large sea level sensitivity and large thickness change projected under RCP4.5 and 8.5 scenarios in the 21st century. Besides, the basins with distinct thickness change projected under two RCP scenarios should also be considered for local sea level projections, since they will likely exert opposite impacts on future sea level change at cities under different greenhouse gas emission scenarios.

4.6 Research limitation and further work

All sea level fingerprints computed by ISSM-SESAW and kernel-based projections are under the assumption that the solid Earth's response to changing ice mass loads is purely elastic. This implies that ISSM-SESAW computation and kernel-based projection are only suitable for ice evolution in a timescale less than one century (Adhikari et al., 2016, Mitrovica et al., 2018). For relative long-timescale loading scenarios (longer than one century), the viscoelastic response of the solid earth should be considered in sea level fingerprint computation. Future studies need to account for this viscoelastic response of the solid earth when providing sea level fingerprints and local sea level contributions for long timescales.

The estimates of future sea level projections in this study are limited by the ice sheet projections they are based upon. In this study, we adopted a single future projection of polar ice sheets under the RCP4.5 and RCP8.5 scenarios in the 21st century, which is currently available to us. However, large uncertainty may exist in future projections in polar ice sheet melting, which can lead to uncertainties when calculating the barystatic sea level change and local sea level contributions at coastal cities. Future studies need to employ more projections of polar ice sheet melting for better sea level projections, like those to-be-released ISMIP6 projections (Seroussi et al., 2020). This is particularly important for calculating local sea level contributions at coastal cities. This is because quantified uncertainties in local sea level contributions by individual polar ice sheet drainage basins are crucial for local stakeholders to guide future coastal planning and scientific research into certain basins.

5. Conclusions

In this research, our goal is to provide high-resolution sea level projections in response to future land ice mass changes over polar ice sheets in the 21st century as a guide to local stakeholders for better mitigation strategies and scientific observations. To this aim, we utilize the unstructured mesh-grid sea level fingerprint module - ISSM-SESAW, developed by NASA/JPL, to provide high-resolution sea level fingerprints in response to each polar ice sheet melting in the 21st century under the RCP4.5 and 8.5 scenarios. In addition, based on ISSM-SESAW, this study explores the sensitivities of sea level fingerprints to different crustal structures in 1-D elastic Earth models and to different resolutions in polar ice sheets. Furthermore, using kernel-based sea level projections, sea level contributions to 10 representative coastal cities by individual drainage basins over polar ice sheets in the 21st century under the RCP4.5 and 8.5 scenarios are also calculated in this study.

The main conclusions are:

1. We demonstrate that sea level fingerprints are insensitive to different crustal structures in 1-D elastic Earth models. It is unnecessary for future study on sea level fingerprints to consider their uncertainty to different 1-D elastic Earth models.
2. We conclude that the resolution at which polar ice sheet mass change is resolved has a significant impact on sea level fingerprints, especially for sea level change in the near field (errors of >20% of the barystatic sea level change). High resolutions (10 km) near to melting sources are crucial for accurate future sea level fingerprints.
3. By 2100, each of the GrIS and AIS melting under the RCP4.5 and 8.5 scenarios will have significant contributions to regional sea level distributions, causing around 70% of the world oceans to have sea-level rise up to 30% different to the barystatic sea level rise.
4. Differences in projections of the AIS melting in the 21st century under the RCP 4.5 and 8.5 scenarios lead to different spatial patterns of regional sea level change not just different magnitudes.

5. Finally, quantifying sea level contributions at coastal cities by individual polar ice sheet drainage basins is important for local stakeholders at coastal cities to better understand future sea level projections. By identifying the most/least contributing ice sources to local sea level rise, a better guidance is provided for local policy and future scientific research.

References

- Adhikari, S., Ivins, E. R., Frederikse, T., Landerer, F. W. and Caron, L. (2019) 'Sea-level fingerprints emergent from GRACE mission data', *Earth Syst. Sci. Data*, 11(2), pp. 629-646.
- Adhikari, S., Ivins, E. R. and Larour, E. (2016) 'ISSM-SESAW v1.0: mesh-based computation of gravitationally consistent sea-level and geodetic signatures caused by cryosphere and climate driven mass change', *Geosci. Model Dev.*, 9(3), pp. 1087-1109.
- Bolch, T., Sandberg Sørensen, L., Simonsen, S. B., Mölg, N., MacHguth, H., Rastner, P. and Paul, F. (2013) 'Mass loss of Greenland's glaciers and ice caps 2003-2008 revealed from ICESat laser altimetry data', *Geophysical Research Letters*, 40(5), pp. 875-881.
- Church, J. A., et al. (2013) 'Sea level change, in Climate Change 2013: The Physical Science Basis. Contribution of Working Group I to the Fifth Assessment Report of the Intergovernmental Panel on Climate Change', edited by T. F. Stocker et al., pp. 1137–1216, *Cambridge Univ. Press*, Cambridge, U. K., and New York.
- Clark, J. A., Farrell, W. E. and Peltier, W. R. (1978) 'Global Changes in Postglacial Sea Level: A Numerical Calculation', *Quaternary Research*, 9(3), pp. 265-287.
- Clark, J. A. and Lingle, C. S. (1977) 'Future sea-level changes due to West Antarctic ice sheet fluctuations', *Nature*, 269(5625), pp. 206-209.
- Conrad, C. P. and Hager, B. H. (1997) 'Spatial variations in the rate of sea level rise caused by the present-day melting of glaciers and ice sheets', *Geophysical Research Letters*, 24(12), pp. 1503-1506.
- Dahlen, F. A. (1976) 'The Passive Influence of the Oceans upon the Rotation of the Earth', *Geophysical Journal International*, 46(2), pp. 363-406.
- Dziewonski, A. M. and Anderson, D. L. (1981) 'Preliminary reference Earth model', *Physics of the Earth and Planetary Interiors*, 25(4), pp. 297-356.

- Farrell, W. E. and Clark, J. A. (1976) 'On Postglacial Sea Level', *Geophysical Journal of the Royal Astronomical Society*, 46(3), pp. 647-667.
- Geuzaine, C. and Remacle, J.-F. (2009) 'Gmsh: A 3-D finite element mesh generator with built-in pre- and post-processing facilities', *International Journal for Numerical Methods in Engineering*, 79(11), pp. 1309-1331.
- Golledge, N. R., Keller, E. D., Gomez, N., Naughten, K. A., Bernales, J., Trusel, L. D. and Edwards, T. L. (2019) 'Global environmental consequences of twenty-first-century ice-sheet melt', *Nature*, 566(7742), pp. 65-72.
- Gomez, N., Mitrovica, J. X., Tamisiea, M. E. and Clark, P. U. (2010) 'A new projection of sea level change in response to collapse of marine sectors of the Antarctic Ice Sheet', *Geophysical Journal International*, 180(2), pp. 623-634.
- Grinsted, A., Jevrejeva, S., Riva, R. E. M. and Dahl-Jensen, D. (2015) 'Sea level rise projections for northern Europe under RCP8.5', *Climate Research*, 64(1), pp. 15-23.
- Hecht, F. (2006) 'BAMG: Bidimensional Anisotropic Mesh Generator, Tech. rep., FreeFem++', *University Pierre et Marie Curie*.
- Holt, T. (2020) *Gauss2lats*: MATLAB Central File Exchange. Available at: <https://www.mathworks.com/matlabcentral/fileexchange/2586-gauss2lats>.
- Jevrejeva, S., Frederikse, T., Kopp, R. E., Le Cozannet, G., Jackson, L. P. and van de Wal, R. S. W. (2019) 'Probabilistic Sea Level Projections at the Coast by 2100', *Surveys in Geophysics*, 40(6), pp. 1673-1696.
- Johnston, P. (1993) 'The effect of spatially non-uniform water loads on prediction of sea-level change', *Geophysical Journal International*, 114(3), pp. 615-634.
- Kendall, R. A., Mitrovica, J. X. and Milne, G. A. (2005) 'On post-glacial sea level – II. Numerical formulation and comparative results on spherically symmetric models', *Geophysical Journal International*, 161(3), pp. 679-706.

- Kennett, B. L. N. and Engdahl, E. R. (1991) 'Traveltimes for global earthquake location and phase identification', *Geophysical Journal International*, 105(2), pp. 429-465.
- Kennett, B. L. N., Engdahl, E. R. and Buland, R. (1995) 'Constraints on seismic velocities in the Earth from traveltimes', *Geophysical Journal International*, 122(1), pp. 108-124.
- Konrad, H., Sasgen, I., Pollard, D. and Klemann, V. (2015) 'Potential of the solid-Earth response for limiting long-term West Antarctic Ice Sheet retreat in a warming climate', *Earth and Planetary Science Letters*, 432, pp. 254-264.
- Kopp, R. E., Horton, R. M., Little, C. M., Mitrovica, J. X., Oppenheimer, M., Rasmussen, D. J., Strauss, B. H. and Tebaldi, C. (2014) 'Probabilistic 21st and 22nd century sea-level projections at a global network of tide-gauge sites', *Earth's Future*, 2(8), pp. 383-406.
- Lambeck, K. (1988) 'The Earth's Variable Rotation: Geophysical Causes and Consequences', *Cambridge Univ. Press*, pp. 449.
- Lambeck, K. and Nakada, M. (1990) 'Late Pleistocene and Holocene sea-level change along the Australian coast', *Palaeogeography, Palaeoclimatology, Palaeoecology*, 89(1), pp. 143-176.
- Larour, E., Ivins, E. R. and Adhikari, S. (2017) 'Should coastal planners have concern over where land ice is melting?', *Science Advances*, 3(11), pp. e1700537.
- Milne, G. A. and Mitrovica, J. X. (1998) 'Postglacial sea-level change on a rotating Earth', *Geophysical Journal International*, 133(1), pp. 1-19.
- Milne, G. A., Mitrovica, J. X. and Davis, J. L. (1999) 'Near-field hydro-isostasy: the implementation of a revised sea-level equation', *Geophysical Journal International*, 139(2), pp. 464-482.
- Mitrovica, J. X., Gomez, N., Morrow, E., Hay, C., Latychev, K. and Tamisiea, M. E. (2011) 'On the robustness of predictions of sea level fingerprints', *Geophysical Journal International*, 187(2), pp. 729-742.

- Mitrovica, J. X., Hay, C. C., Kopp, R. E., Harig, C. and Latychev, K. (2018) 'Quantifying the Sensitivity of Sea Level Change in Coastal Localities to the Geometry of Polar Ice Mass Flux', *Journal of Climate*, 31(9), pp. 3701-3709.
- Mitrovica, J. X. and Peltier, W. R. (1991) 'On postglacial geoid subsidence over the equatorial oceans', *Journal of Geophysical Research: Solid Earth*, 96(B12), pp. 20053-20071.
- Mitrovica, J. X., Tamisiea, M. E., Davis, J. L. and Milne, G. A. (2001) 'Recent mass balance of polar ice sheets inferred from patterns of global sea-level change', *Nature*, 409(6823), pp. 1026-1029.
- Munk, W. H. and Macdonald, G. J. F. (1960) 'The Rotation of the Earth', *Cambridge University Press*.
- Peltier, W. R. (1994) 'Ice Age Paleotopography', *Science*, 265(5169), pp. 195-201.
- Plag, H.-P. (2006) 'Recent relative sea-level trends: an attempt to quantify the forcing factors', *Philosophical Transactions of the Royal Society A: Mathematical, Physical and Engineering Sciences*, 364(1841), pp. 821-844.
- Quinn, K. J., Ponte, R. M. and Tamisiea, M. E. (2015) 'Impact of self-attraction and loading on Earth rotation', *Journal of Geophysical Research: Solid Earth*, 120(6), pp. 4510-4521.
- Rignot, E., Mouginot, J., Scheuchl, B., van den Broeke, M., van Wessem, M. J. and Morlighem, M. (2019) 'Four decades of Antarctic Ice Sheet mass balance from 1979–2017', *Proceedings of the National Academy of Sciences*, 116(4), pp. 1095-1103.
- Riva, R. E. M., Frederikse, T., King, M. A., Marzeion, B. and van den Broeke, M. R. (2017) 'Brief communication: The global signature of post-1900 land ice wastage on vertical land motion', *The Cryosphere*, 11(3), pp. 1327-1332.
- Schröder, L., Horwath, M., Dietrich, R., Helm, V., van den Broeke, M. R. and Ligtenberg, S. R. M. (2019) 'Four decades of Antarctic surface elevation changes from multi-mission satellite altimetry', *The Cryosphere*, 13(2), pp. 427-449.

- Seroussi, H., Nowicki, S., Payne, A. J., Goelzer, H., Lipscomb, W. H., Abe Ouchi, A., Agosta, C., Albrecht, T., Asay-Davis, X., Barthel, A., Calov, R., Cullather, R., Dumas, C., Gladstone, R., Golledge, N., Gregory, J. M., Greve, R., Hatterman, T., Hoffman, M. J., Humbert, A., Huybrechts, P., Jourdain, N. C., Kleiner, T., Larour, E., Leguy, G. R., Lowry, D. P., Little, C. M., Morlighem, M., Pattyn, F., Pelle, T., Price, S. F., Quiquet, A., Reese, R., Schlegel, N. J., Shepherd, A., Simon, E., Smith, R. S., Straneo, F., Sun, S., Trusel, L. D., Van Breedam, J., van de Wal, R. S. W., Winkelmann, R., Zhao, C., Zhang, T. and Zwinger, T. (2020) 'ISMIP6 Antarctica: a multi-model ensemble of the Antarctic ice sheet evolution over the 21st century', *The Cryosphere Discuss.*, 2020, pp. 1-54.
- Shepherd, A., Gilbert, L., Muir, A. S., Konrad, H., McMillan, M., Slater, T., Briggs, K. H., Sundal, A. V., Hogg, A. E. and Engdahl, M. E. (2019) 'Trends in Antarctic Ice Sheet Elevation and Mass', *Geophysical Research Letters*, 46(14), pp. 8174-8183.
- Smith, B., Fricker, H. A., Gardner, A. S., Medley, B., Nilsson, J., Paolo, F. S., Holschuh, N., Adusumilli, S., Brunt, K., Csatho, B., Harbeck, K., Markus, T., Neumann, T., Siegfried, M. R. and Zwally, H. J. (2020) 'Pervasive ice sheet mass loss reflects competing ocean and atmosphere processes', *Science*, 368(6496), pp. 1239-1242.
- Tamisiea, M. E., Mitrovica, J. X., Milne, G. A. and Davis, J. L. (2001) 'Global geoid and sea level changes due to present-day ice mass fluctuations', *Journal of Geophysical Research: Solid Earth*, 106(B12), pp. 30849-30863.
- Tamtsiea, M. E., Mitrovica, J. X., Davis, J. L. and Milne, G. A. (2003) 'II: SOLID EARTH PHYSICS: Long Wavelength Sea Level and Solid Surface Perturbations Driven by Polar Ice Mass Variations: Fingerprinting Greenland and Antarctic Ice Sheet Flux', *Space Science Reviews*, 108(1), pp. 81-93.
- Wahr, J. M. (1985) 'Deformation induced by polar motion', *Journal of Geophysical Research: Solid Earth*, 90(B11), pp. 9363-9368.

- Wang, H., Xiang, L., Jia, L., Jiang, L., Wang, Z., Hu, B. and Gao, P. (2012) 'Load Love numbers and Green's functions for elastic Earth models PREM, iasp91, ak135, and modified models with refined crustal structure from Crust 2.0', *Computers & Geosciences*, 49, pp. 190-199.
- Wessel, P., Smith, W. H. F., Scharroo, R., Luis, J. and Wobbe, F. (2013) 'Generic Mapping Tools: Improved Version Released', *Eos, Transactions American Geophysical Union*, 94(45), pp. 409-410.
- Woodward, R. S. (1888) 'On the form and position of the sea level with special references to its dependence on superficial masses symmetrically disposed about a normal to the earth's surface', *US Geol. Surv. Bull.*, pp. 87-170.
- Wouters, B., Bonin, J. A., Chambers, D. P., Riva, R. E., Sasgen, I. and Wahr, J. (2014) 'GRACE, time-varying gravity, Earth system dynamics and climate change', *Rep Prog Phys*, 77(11), pp. 116801.
- Zwally, H. J., Mario, B. G., Matthew, A. B. and Jack, L. S. (2012) 'Antarctic and Greenland Drainage Systems', *GSFC Cryospheric Sciences Laboratory*.